

# Electronic properties and applications of MXenes: a theoretical review

Mohammad Khazaei,<sup>1</sup> Ahmad Ranjbar,<sup>1</sup> Masao Arai,<sup>2</sup> Taizo Sasaki,<sup>2</sup> and Seiji Yunoki<sup>1,3,4</sup>

<sup>1</sup>Computational Materials Science Research Team, RIKEN Advanced Institute for Computational Science (AICS), Kobe, Hyogo 650-0047, Japan

<sup>2</sup>International Center for Materials Nanoarchitectonics, National Institute for Materials Science (NIMS), 1-1 Namiki, Tsukuba 305-0044, Ibaraki, Japan

<sup>3</sup>Computational Condensed Matter Physics Laboratory, RIKEN, Wako, Saitama 351-0198, Japan

<sup>4</sup>Computational Quantum Matter Research Team, RIKEN Center for Emergent Matter Science (CEMS), Wako, Saitama 351-0198, Japan

(Dated: February 27, 2017)

Recent chemical exfoliation of layered MAX phase compounds to novel two-dimensional transition metal carbides and nitrides, so called MXenes, has brought new opportunity to materials science and technology. This review highlights the computational attempts that have been made to understand the physics and chemistry of this very promising family of advanced two-dimensional materials, and to exploit their novel and exceptional properties for electronic and energy harvesting applications.

## I. INTRODUCTION

It has been demonstrated in recent extensive studies that low-dimensional systems containing transition metals with open  $d$ -orbital shells may exhibit a multitude of interesting properties because of different oxidation and spin states, and relatively large spin-orbit coupling of the transition metals. Hence, transition metal-based low-dimensional systems provide an excellent ground for exploring and exploiting the internal degrees of freedom of electrons – charge, orbital, and spin – and their interplay for fundamental research and device applications [1–4]. There are many transition metal-based low dimensional systems in the literature, e.g. dichalcogenides, which have been or may potentially be exfoliated in the experiments [5, 6]. Among them, nowadays, MXenes [7, 8] are truly at the cutting edge of materials research and promise new scientific and technological horizons.

MXenes [7, 8] are a new class of two-dimensional (2D) transition metal carbides and nitrides with chemical formula of  $M_{n+1}X_n$  ( $M = \text{Sc, Ti, V, Cr, Zr, Nb, Mo, Hf, Ta}$ ;  $X = \text{C, N}$ ;  $n=1-3$ ) that have recently been synthesized through etching MAX phases [9–14]. These 2D systems have been named as MXenes because they originate from the MAX phases by removing “A” elements and because they are structurally analogous to graphene [7, 8]. Very recently, significant progress in the growth of high quality crystalline MXenes has been achieved by the chemical vapor deposition technique [15, 16]. Moreover, the family of MXenes has been lately expanded to ordered double transition metals carbides  $M'_2M''C_2$  and  $M'_2M''C_3$  [17]. Considering the large number of compositional variety of the MAX phase compounds, a large number of 2D MXenes with unprecedented properties is expected to be produced.

Experimentally, MXenes have already found applications as transparent conductors [18–20], field effect transistors [21], supercapacitors [22–24], Li ion batteries [25, 26], electromagnetic interface shielders [27], fillers in polymeric composites [28], hybrid nanocomposites [29], purifiers [30, 31], dual-responsive surfaces [32], suitable substrates for dyes [33], catalysts [34, 35], promising materials for methane storage [36], and photocatalysts for hydrogen production [37],

as well as being ceramic biomaterials with high photothermal conversion efficiency for cancer therapy [38]. Theoretically, many applications have been proposed for MXenes in electronic [39–43], magnetic [44–48], optical [49, 50], thermoelectric [51–56], and sensing devices [57], as well as being new potential materials for catalytic and photocatalytic reactions [58–63], hydrogen storage media [64, 65], and nanoscale superconductivity [66]. Some of MXenes are predicted to be topological insulators with large band gaps involving only  $d$  orbitals [67–71]. MXenes are also expected to be used as ultralow work function materials [72] and Schottky barrier junctions [73–76].

As the experimental and theoretical studies described above have already suggested, MXenes are appealing 2D systems because of the following reasons. 1) Owing to their ceramic nature, MXenes are chemically and mechanically stable. 2) MXenes can be found in different forms of monolayer, few layers, and multilayers. 3) MXenes can be synthesized as complex materials made of mixture of light and heavy transition metals, which makes it possible to tune the number of valence electrons and the relativistic spin-orbit coupling (SOC). This enhances their electronic functionality and mechanical stability. 4) The thickness of MXene monolayers is controllable. This allows us to examine the quantum confinement related phenomena. 5) The surfaces of MXenes can be functionalized with various chemical groups, which offers possibilities for surface state engineering. 6) Similar to graphene, some of MXenes exhibit massless Dirac dispersions in their band structures near the Fermi level [67–70, 77]. This opens broad possibilities for Dirac-based physics and applications [67–70]. These properties make MXenes unique among other known 2D materials although some of them have not been experimentally observed yet.

This article reviews the current status of theoretical studies on MXenes, highlighting the recent progress based on first-principles calculations. It updates and comprehends the previous excellent theoretical reviews in Refs. [78, 79] by providing insights into many physical and chemical characteristics and applications of MXenes. For the experimental progresses on MXenes, one can find comprehensive reviews in Refs. [80–84]. The rest of this review is organized as follows. Sec. II summarizes computational methods employed to obtain the

theoretical results discussed in this review. Sec. III briefly discusses the structural, mechanical, and electronic properties of the parent structures of MXenes, *i.e.*, MAX phases. Sec. IV explains first why the surfaces of 2D MXenes are usually saturated with chemical groups. Then, the effects of surface functionalization on mechanical, electronic, magnetic, optical, transport, and surfaces states of MXenes are discussed. Some of the proposed applications of 2D MXenes as low work function electron emitters, catalyst for hydrogen evolution, promising thermoelectric materials, and energy storage media are also described. Sec. V summarizes the electronic structures of MXenes in the form of nanoribbons, nanotubes and heterostructures. Finally, outlook for future research on MXenes is provided in Sec. VI.

## II. COMPUTATIONAL METHODS

Before discussing the properties and applications of MXenes, it is worth summarizing briefly computational methods employed in the following theoretical studies of this review. Among different methods, density functional theory (DFT) has proven to be a reliable method to predict various physical and chemical phenomena in atomic scale. Hence, DFT calculations are performed to examine many properties and applications of MXenes. However, it is known that the simple DFT method may fail in predicting the values of band gap and van der Waals interaction, and properties of strongly correlated materials. For instance, the Perdew-Burke-Ernzerhof (PBE) version of the generalized gradient approximation (GGA) for the exchange-correlation functional [85], which is most of often used in this review, underestimates the band gap. Hence, in some of the studies discussed below, the hybrid functional [Heyd-Scuseria-Ernzerhof (HSE06)] [86, 87] is employed to improve the estimation of the band gap, and the semi-empirical DFT-D2 method (Grimme method) [88] is used to treat properly the Van der Waals interaction. Furthermore, the DFT+U method [89, 90] is applied to correctly obtain magnetic order when the electron correlation in transition metals is important. Because of the approximate nature of the DFT-based methods [91], this review mainly focuses on the general trends, which are expected in the physics and chemistry of MXenes, rather than emphasizing quantitatively the exact values of various properties. In the following, the DFT-PBE method is employed for the theoretical studies, unless otherwise stated.

## III. MAX PHASES

MAX phases are a large family of hexagonal layered ceramic compounds with symmetry group of  $P6_3/mmc$  and with chemical formula of  $M_{n+1}AX_n$  ( $n=1-3$ ), where “M”, “A”, and “X” represent an early transition metal (Sc, Ti, V, Cr, Zr, Nb, Mo, Hf, and Ta), an element from groups 13–16 (Al, Si, P, S, Ga, Ge, As, In, and Sn) in the periodic table, and carbon and/or nitrogen, respectively [9–14]. Figure 1(a) shows the typical crystal structure of  $M_2AX$  MAX phase compounds.

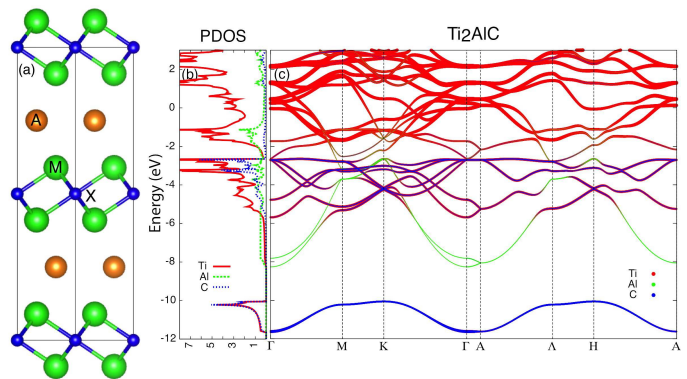


FIG. 1. (a) Typical structure of  $M_2AX$  MAX phases. (b) Projected density of states [PDOS (states/eV/cell)] and (c) projected band structure of  $Ti_2AlC$  [12]. For clarity, the PDOS for Al is scaled by factor 3. The Fermi energy is located at zero energy.  $\Gamma(0,0,0)$ ,  $M(1/2,0,0)$ ,  $K(1/3,1/3,0)$ ,  $A(0,0,1/2)$ ,  $\Lambda(1/2,0,1/2)$ , and  $H(1/3,1/3,1/2)$  are high symmetric momenta in the Brillouin zone of  $Ti_2AlC$ .

Over 60 different MAX phase compounds have already been synthesized experimentally [10, 11]. MAX phases typically exhibit favorable properties of ceramics such as high structural stiffness, and also favorable properties of metals such as good electrical and thermal conductivity [12]. MAX phases have potential applications such as wear and corrosion protection, heat exchangers, lubricants, nozzles, and kiln furniture [10, 11].

Based on first-principles calculations, elastic constants of more than 240 different  $M_2AC$  and  $M_2AN$  compounds with various M and A elements have been theoretically studied so far [9]. Among these, many of the compounds are found to satisfy the mechanical stability criteria for hexagonal structures:  $C_{11} > |C_{12}|$ ,  $C_{66} > 0$ , and  $(C_{11} + C_{12})C_{33} - 2C_{13}^2 > 0$ , where  $C_{ij}$  is the second rank tensor of elastic constant [92]. Therefore, many of them are elastically stable and have a great chance to be realized under appropriate experimental conditions. Another computational screening study has analyzed the formation energies of 216 pure  $M_2AX$  compounds and 10314 solid solution  $(MM')_2(AA')(XX')$  [14], and found that 3140 compounds, including 49 experimentally known  $M_2AX$  phases, exhibit formation energies of less than  $-30$  meV/atom. A significant subsets of 301 compositions with formation energy lower than  $-100$  meV/atom exhibit favorable synthesis conditions.

Recently, the family of MAX phases has also been theoretically extended to  $M_2AlB$  compounds [12]. The formation energy ( $E_f$ ) calculations find that  $E_f(M_2AlN) \downarrow E_f(M_2AlC) \downarrow E_f(M_2AlB)$  [12]. This indicates that the  $M_2AlN$  phases will likely be obtained with higher purity in experiments. This trend of the formation energies for MAX phases is understood by considering several entangled factors, *i.e.*, 1) the strength of hybridization between  $d$  orbitals of M and others ( $p$  orbitals of Al, and  $s$  and  $p$  orbitals of X), 2) the number of valence electrons that fill bonding, nonbonding, and antibonding states, and 3) the required energy for volume expansion of the

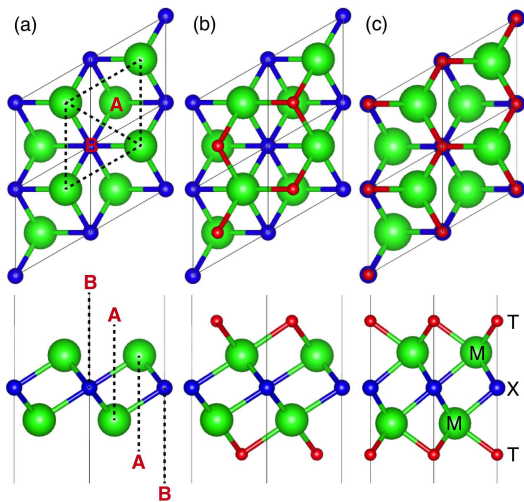


FIG. 2. Top and side views of (a) pristine MXene  $M_2X$ . Top and side views of (b) model 2 and (c) model 4 for functionalized MXene (see the text). A and B indicate different types of hollow sites in (a). M, X, and T denote transition metal (green), C/N (blue), and attached chemical groups such as F, O, and OH (red), respectively.

transition metals to host the X elements [12].

The first-principles calculations find that  $M_2AlB$ ,  $M_2AlC$ , and  $M_2AlN$  are all metallic [12]. As shown in Figs. 1(b) and 1(c) for  $Ti_2AlC$ , the states around the Fermi energy of these compounds are mainly dominated by  $d$  orbitals of the transition metals. The common features of hybridization are evident in these compounds, where bonding (antibonding) states between  $d$  orbitals of M and  $p$  orbitals of Al or  $p$  orbitals of X are located below (above) the Fermi energy. Between these bonding and antibonding states, nonbonding states of M are located near the Fermi energy. More detailed analysis shows that the number of valence electrons per unit cell (valence electron concentration), which fill the bonding and antibonding states, can affect and control the formation energy and the mechanical property of MAX phases significantly [12].

#### IV. 2D MXENES

2D MXenes are experimentally obtained when the “A” element is washed out from the MAX phases upon applying appropriate acid solution such as HF [7, 8]. This is possible because in some of the MAX phases the bonding between elements A and M is weaker than those between elements M and X. However, it is experimentally observed that the outer layers are often saturated with F, O, and/or OH groups when MXenes are chemically exfoliated by HF acid solutions to eliminate the “A” element [93–97].

The exfoliation process of  $Ti_3AlC_2$  to  $Ti_3C_2$  has been theoretically studied in the presence of water and HF acid using *ab initio* molecular dynamics simulations [98, 99]. There, it is shown that the spontaneous dissociation of HF and subsequent termination with H or F at the edge of Ti atoms make Al-M bonding weak, consequently opening the interlayer gap.

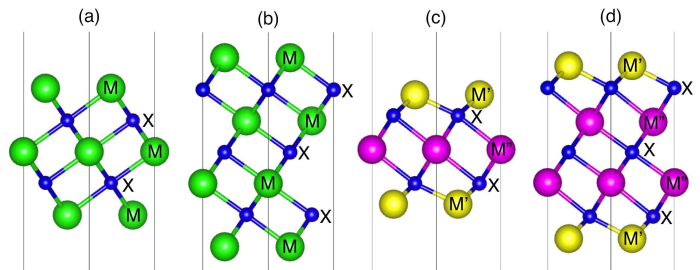


FIG. 3. Side views of pristine (a)  $M_3X_2$ , (b)  $M_4X_3$ , (c)  $M_2M'X_2$ , and (d)  $M_2M'_2X_3$  MXenes, where M, M', and M'' denote transition metals, and X represents C or N.

The further insertion of HF is facilitated through the interlayer gap. This leads to the formation of  $AlF_3$  and  $H_2$ , which eventually come out of the MAX phase. After these processes, the fluorinated MXene leaves behind [98, 99].

Experimentally, MXenes of  $Ti_2C$  [8],  $V_2C$  [25],  $Nb_2C$  [25],  $Mo_2C$  [100],  $Ti_3C_2$  [7],  $Zr_3C_2$  [101],  $Nb_4C_3$  [102],  $Ta_4C_3$  [8], and  $Ti_4N_3$  [103] as well as  $TiNbC$  [8],  $(Ti_{0.5}Nb_{0.5})_2C$  [8],  $(V_{0.5}Cr_{0.5})_3C_2$  [8],  $Ti_3CN$  [8],  $Mo_2TiC_2$  [17],  $Mo_2ScC_2$  [104],  $Cr_2TiC_2$  [17],  $Mo_2Ti_2C_3$  [17],  $(Nb_{0.8}Ti_{0.2})_4C_3$  [102], and  $(Nb_{0.8}Zr_{0.2})_4C_3$  [102] have already been synthesized. There are comprehensive reviews on synthesis and current experimental status of MXenes [80–84]. The crystal structures of 2D  $M_2X$ ,  $M_3X_2$ ,  $M_4X_3$ ,  $M_2M'X_2$ , and  $M_2M'_2X_3$  are shown in Figs. 2 and 3.

#### A. Structural and mechanical properties

The model structures for 2D MXene systems can be constructed by removing “A” element from the bulk MAX phases. Since the MAX phases have hexagonal symmetry, the derived MXene systems form hexagonal lattices with the same symmetry. As schematically shown in Fig. 2(a), 2D  $M_2X$  MXene consists of trilayer sheets with a hexagonal-like unit cell, where the “X” layer is sandwiched by two “M” transition metal layers. Since the coordination number of a transition metal ion is often six, it is natural to assume that the transition metals in MXenes make six chemical bonds with the neighboring X atoms and the attached chemical groups on the surfaces, resulting in the formation of  $M_2XF_2$ ,  $M_2X(OH)_2$ , and  $M_2XO_2$  [39].

On the surfaces of  $M_2X$ , two types of hollow sites exist: hollow sites (A) under which there is no “X” atom between the transition metal layers and hollow sites (B) under which there is a “X” atom, as indicated in the lower panel of Fig. 2(a). Therefore, depending on the relative positions of the termination groups attached to the transition metal atoms, four different configurations are possible for the chemical termination of the  $M_2X$  system. Model 1: two functional groups locate on top of the two transition metals. Model 2: two functional groups are on top of hollow sites A. Model 3: one of the functional groups locates on top of a hollow site A and the other functional group locates on top of a hollow site B. Model 4: the two functional groups locate on top of hollow sites B. Fig-

ures 2(b) and 2(c) show the schematic top and side views of models 2 and 4, respectively.

These four models should be considered for each type of functional groups with fully relaxing atomic positions to determine the most stable structure. As a general trend in functionalized MXenes, model 1 is energetically less stable than other three models and in many cases it is transformed to one of models 2–4 during structure optimization. It is also found that the relative structural stabilities of models 2–4 depend mainly on possible ionic state(s) of the transition metals on the surfaces [39]. If the transition metals can provide sufficient electrons to both X and the attached functional groups, model 2 becomes the most stable configuration [39]. Otherwise, either model 3 or model 4 is a more stable configuration [39].

In order to understand the stability of functionalized MXenes, the formation energy has to be evaluated. First-principles calculations find that MXenes can gain a very large amount of negative formation energy when the surfaces are functionalized [39]. This indicates the formation of strong bonds between the transition metals and the attached groups, which encourages synthesizing MXenes with particular surface functionalization [39]. It has also been examined whether the surfaces of fully functionalized MXene are thermodynamically more favorable than those of less functionalized MXene [39, 105]. It is indeed shown theoretically that the surfaces are fully functionalized at particular chemical potentials in some of the MXene systems [39, 105]. Phonon frequency analyses have proved that many of these MXenes with full surface functionalization are locally stable [39, 68, 72, 106, 107]. Therefore, various fully functionalized MXenes can be realized experimentally in appropriate conditions although there are still some challenges.

The effect of surface functionalization on elastic constant  $C_{11}$  of MXenes have been studied using first-principles calculations [108, 109]. It is found that oxygen functionalized MXenes exhibit smaller lattice parameters and larger  $C_{11}$  as compared to those functionalized with F or OH [109]. This is due to the stronger bonding between O and surface transition metals.

In another theoretical study, the thickness dependence of mechanical properties of pristine 2D  $Ti_{n+1}C_n$  ( $n=1, 2, \text{ and } 3$ ) has been investigated using molecular dynamics simulations. The Young's modulus, extracted from the slope of strain-stress curves, are found to be 597, 502, and 534 GPa for  $Ti_2C$ ,  $Ti_3C_2$ , and  $Ti_4C_3$ , respectively [110], and thus it is the highest for the thinnest MXene. It is also observed that  $Ti_2C$  and  $Ti_3C_2$  show similar behavior under high tensile stress: the bond breaking begins in the outermost regions of the layer at the point of the highest local stress and propagates deeper into the center of the system. The crack propagation in these systems is accompanied by crumpling and folding of the layer near the growing gap [110]. In contrast, cracks in  $Ti_4C_3$  occur first in the central region of the layer. At larger stress, these cracks grow in size, leading to the complete fracture of the sample with the formation of several  $Ti_4C_3$  fragments [110].

The effect of F, OH, and O functionalization on the response of  $Ti_{n+1}C_n$  ( $n=1, 2, \text{ and } 3$ ) to the tensile stress has

also been investigated theoretically to show that  $Ti_2CO_2$  can sustain large strain under biaxial and uniaxial tension much better than graphene [111]. On the other hand, the pristine 2D  $Ti_{n+1}C_n$  ( $n=1, 2, \text{ and } 3$ ) is vulnerable against the tensile strain because the surface atomic layer collapses easily. However, the surface functionalization can slow down this collapse and thus improves the mechanical flexibility [111]. The unique strengthening by oxygen functionalization is attributed to the significant charge transfer from the inner Ti-C bonds to the outer Ti-O surface ones [112].

Although the F, O, and OH terminations weaken the interlayer coupling as compared with the pristine counterparts, the interlayer coupling is still significantly stronger than van der Waals bonding as specified by the fact that the binding energies of stacked  $Ti_{n+1}C_nT_2$  ( $T = F, OH, \text{ or } O$ ) are 2–6 times larger than those of well-known graphite and  $MoS_2$  with weak interlayer coupling [113]. Therefore, the successful exfoliation of stacked  $Ti_{n+1}C_nT_2$  with binding energies in the range of 1–1.33 Jm<sup>-2</sup> into monolayers invariably requires further weakening of the interlayer coupling [113]. The interlayer coupling in the OH-terminated  $Ti_{n+1}C_n$  is stronger than that in the F- or O-terminated one because of the formation of hydrogen bonds between the layers in the former [113].

It should be noted that the experimentally obtained MXenes are not structurally perfect. The recent scanning transmission electron microscopy (STEM) and electron energy loss spectroscopy (EELS) experiments show that point defects are present on the surfaces that can affect the local surface chemistry [114, 115]. The defects are formed when the surface transition metals are etched/removed by the HF in the etchant solution. Thus, changing the HF concentration in the etchant should vary the defect concentration [115]. This gives us the ability to control the surface properties for catalytic, energy storage, and other applications. However, the existence of a defect does not affect significantly the metallic properties of MXenes [115].

Although MXenes are made by chemical exfoliation of MAX phases, their synthesis through mechanical exfoliation of MAX phases may also be possible. This is because in some of the MAX phases elastic constants satisfy  $C_{11} < C_{33}$ , which indicates that the overall bondings along the  $ab$  plane is stronger than the  $c$  direction [12, 13, 116]. Therefore, if  $C_{33}$  is smaller than  $C_{11}$ , it might be more feasible to break the M–A–M bonds under appropriate mechanical tension without significantly damaging the M–X–M bonds [12, 13].

## B. Electronic properties

Similar to the MAX phases, the pristine MXenes are all metallic. However, upon surface functionalization, some of the MXenes become semiconducting. As will be discussed below, theoretical investigations have shown that the MXenes can be divided into two categories, topologically trivial [39] and nontrivial [67–71] metal/semimetal or semiconductor, depending on the strength of relativistic SOC in these systems.

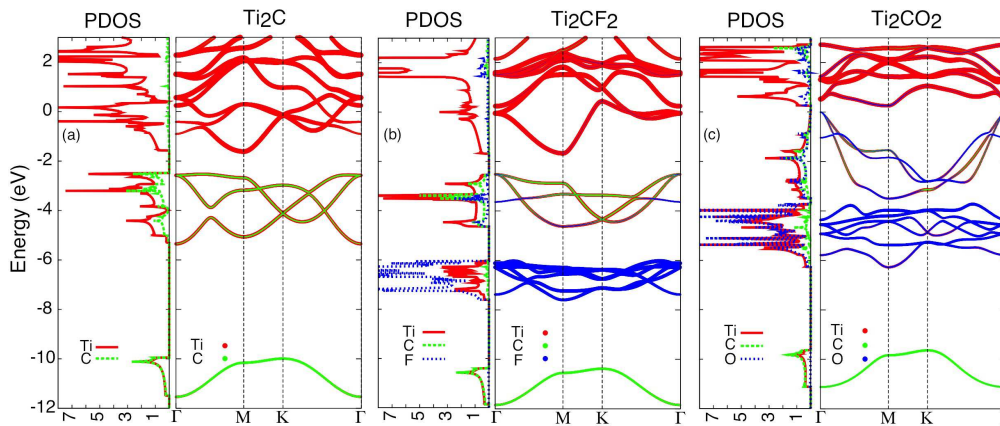


FIG. 4. Projected density of states [PDOS (states/eV/cell)] and projected band structures for (a)  $\text{Ti}_2\text{C}$ , (b)  $\text{Ti}_2\text{CF}_2$ , and (c)  $\text{Ti}_2\text{CO}_2$  [39]. The Fermi energy is located at zero energy.

### 1. Topologically trivial metals and semiconductors

While most of the functionalized MXenes are metallic,  $\text{Sc}_2\text{CT}_2$  ( $T = \text{F, OH, and O}$ ),  $\text{Ti}_2\text{CO}_2$ ,  $\text{Zr}_2\text{CO}_2$ , and  $\text{Hf}_2\text{CO}_2$  become semiconducting with the surface functionalization. The energy gaps are estimated to be 1.03, 0.45, and 1.8 eV for  $\text{Sc}_2\text{CT}_2$  with  $T = \text{F, OH, and O}$ , respectively, 0.24 eV for  $\text{Ti}_2\text{CO}_2$ , 0.88 eV for  $\text{Zr}_2\text{CO}_2$ , and 1.0 eV for  $\text{Hf}_2\text{CO}_2$  within general gradient approximation (GGA) [39]. The band structure calculations reveal that  $\text{Sc}_2\text{C}(\text{OH})_2$  has a direct band gap and the other semiconductors have indirect band gaps. Since Ti, Zr, and Hf are in the same group in the periodic table with the same number of electrons in the outermost partially filled atomic orbital shell ( $[\text{Ar}]3d^24s^2$ ,  $[\text{Kr}]4d^25s^2$ , and  $[\text{Xe}]4f^{14}5d^26s^2$ ), the corresponding MXene systems exhibit the similar metallic to semiconducting behavior upon the same type of functionalization. It is also predicted that both F and OH groups affect similarly the electronic structure of a pristine MXene system [39]. This is simply because each F or OH group is capable of receiving only one electron from the surfaces. By the same token, the O group differs from the F and OH groups because it demands two electrons from the surfaces to be stabilized [39].

In order to understand why some of the MXenes become semiconducting, the electronic structures of MXenes with and without the surface functionalizations have been systematically studied [39]. The calculations show that pristine  $\text{M}_2\text{X}$  ( $X = \text{C or N}$ ) systems are all metallic with the Fermi energy locating at the  $d$  bands of transition metal M. In most MXenes, the  $p$  bands of carbon/nitrogen X appear below the  $d$  bands separated by a small band gap. With the F, OH, or O functionalization, new bands are generated below the Fermi energy, resulting from F or O  $p$  orbitals hybridized with M  $d$  orbitals.  $\text{Sc}_2\text{CT}_2$  ( $T = \text{F, OH, or O}$ ),  $\text{Ti}_2\text{CO}_2$ ,  $\text{Zr}_2\text{CO}_2$ , and  $\text{Hf}_2\text{CO}_2$  turn to be semiconducting because the functionalization shifts the Fermi energy to the center of the gap between M  $d$  bands and X  $p$  bands. As examples, Fig. 4 shows the projected density of states and projected band structures for  $\text{Ti}_2\text{C}$ ,  $\text{Ti}_2\text{CF}_2$ , and  $\text{Ti}_2\text{CO}_2$ . It has also been shown that the band gap

of  $\text{Ti}_2\text{CO}_2$  and  $\text{Sc}_2\text{CO}_2$  can be significantly varied by applying either strain [117, 118] or external electric field [119, 120].

### 2. Topologically non-trivial semimetals and semiconductors

Since many of MXenes contain heavy  $4d$  and  $5d$  transition metals, the relativistic SOC affects the electronic structures significantly. As shown in Fig. 5, without considering the SOC,  $\text{M}_2\text{CO}_2$  ( $M = \text{Mo, W}$ ) and  $\text{M}'_2\text{M}''\text{C}_2\text{O}_2$  ( $M' = \text{Mo, W}$ ;  $M'' = \text{Ti, Zr, W}$ ) are semiconducting with a zero energy gap (semimetallic) because the topmost valence band and the lowest conduction band touch only at the  $\Gamma$  point, around which the valence and conduction bands are both parabolic. The projected band structure calculations reveal that the bands near the Fermi energy originate from  $d$  orbitals of transition metals M, or  $M'$  and  $M''$ . Upon considering the SOC, the degeneracy of the topmost valence band and the lowest conduction band at the Fermi energy is lifted and the band gap is open at the  $\Gamma$  point (see lower panels in Fig. 5). Consequently,  $\text{M}_2\text{CO}_2$  and  $\text{M}'_2\text{M}''\text{C}_2\text{O}_2$  turn into semiconductors with indirect band gaps [67, 68]. The induced band gap is larger as the SOC is larger [68]. It is found that the band gaps can be as large as 0.194 eV (0.472 eV) for  $\text{W}_2\text{CO}_2$  and 0.285 (0.401 eV) for  $\text{W}_2\text{HfC}_2\text{O}_2$  within the generalized gradient approximation (hybrid functional HSE06) [67, 68]. Although the similar features are observed for  $\text{M}'_2\text{M}''\text{C}_3\text{O}_2$  ( $M' = \text{Mo, W}$ ;  $M'' = \text{Ti, Zr, Hf}$ ), these systems are still semimetallic even with considering the SOC (see the rightmost panels in Fig. 5) [68].

The SOC lifts the degeneracy of the bands at the  $\Gamma$  point by inducing a finite gap. The nature of these bands around the Fermi energy can be characterized by the  $Z_2$  topological invariant. Since all the  $\text{M}_2\text{CO}_2$ ,  $\text{M}'_2\text{M}''\text{C}_2\text{O}_2$ , and  $\text{M}'_2\text{M}''\text{C}_3\text{O}_2$  MXenes have the inversion symmetry, the  $Z_2$  topological invariant can be simply calculated from the parity of the valence band wave functions at the time reversal invariant momentum (TRIM) points of the Brillouin zone [121, 122]. For the hexagonal structure, the TRIM points are located at  $\Gamma$ :  $\mathbf{k}_1 = (0, 0)$ ,  $M_1$ :  $\mathbf{k}_2 = (0, 0.5)$ ,  $M_2$ :  $\mathbf{k}_3 = (0.5, 0)$ , and

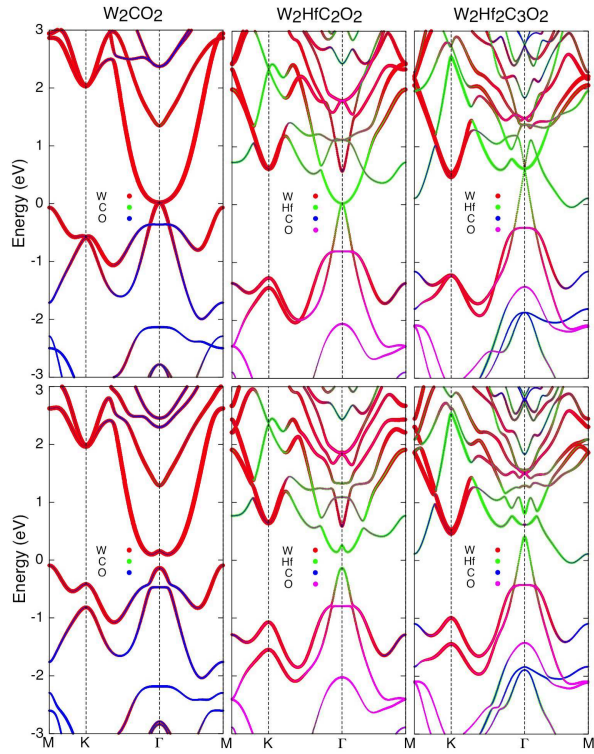


FIG. 5. Top (bottom) panels: projected band structures for  $W_2CO_2$ ,  $W_2HfC_2O_2$ , and  $W_2Hf_2C_3O_2$  calculated without (with) the relativistic spin-orbit coupling [67, 68]. The Fermi energy is located at zero energy.

$M_3$ :  $\mathbf{k}_4 = (0.5, 0.5)$ , and therefore the  $Z_2$  index  $\nu (= 0, 1)$  is evaluated by  $(-1)^\nu = \prod_{i=1}^4 \delta(\mathbf{k}_i)$ , where  $\delta(\mathbf{k}_i) = \prod_{n=1}^N \eta_n(\mathbf{k}_i)$ ,  $\eta_n(\mathbf{k}_i) (= \pm 1)$  is the parity of the  $n$ th valence band at TRIM  $\mathbf{k}_i$ , and  $N$  is the number of the occupied valence bands [121, 122]. The trivial and nontrivial topological phases are identified with  $\nu = 0$  and 1, respectively. The parity analysis of the occupied bands at the TRIM points finds that  $\nu = 1$  for all the systems discussed here, and therefore  $M_2CO_2$  ( $M = Mo, W$ ) and  $M'_2M''C_2O_2$  ( $M' = Mo, W$ ;  $M'' = Ti, Zr, Hf$ ) are topological insulator and  $M'_2M'_2C_3O_2$  are topological semimetal [67, 68]. The 2D topological insulators display intriguing conducting edge states in which electrons with opposite spins propagate in the opposite directions and thus they are robust against non-magnetic impurities and disorders [123–126]. It should also be emphasized that the band inversion occurs in these topologically non-trivial MXenes mostly among  $d$  orbitals (more precisely,  $d_z$  and  $d_{xy}/d_{x^2-y^2}$  orbitals) of the transition metals [67, 68], not involving  $s$  and  $p$  orbitals as in the previously known or predicted topological insulators [123–126].

### C. Surface state properties

The careful examination of the projected band structures of the OH-terminated MXenes has revealed that some of the states around the  $\Gamma$  point, near and above the Fermi energy, do not constitute any of the composed elements [42]. As

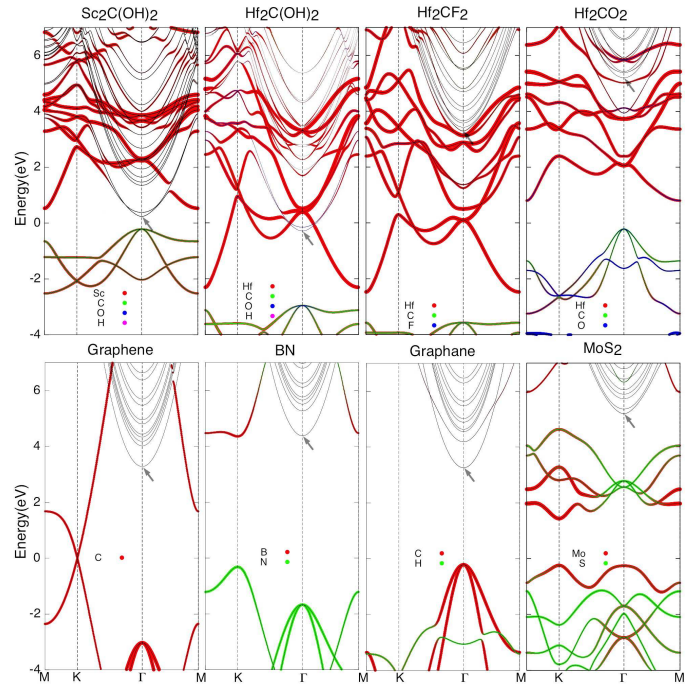


FIG. 6. Projected band structures onto each constituent atoms for eight different systems indicated in the figures [42]. The position of the lowest energy nearly free state (NFE) near the Fermi energy at the  $\Gamma$  point is indicated by arrow. The Fermi energy is located at zero energy.

examples, the projected band structures of  $Sc_2C(OH)_2$  and  $Hf_2C(OH)_2$  are shown in Fig. 6. These states mainly distribute in the vacuum region outside the hydrogen atoms and, more interestingly, they have nearly free electron (NFE) characteristics with parabolic energy dispersions with respect to the crystal wave vector [42].

The electron localization function (ELF) analysis [127] in Fig. 7 shows clearly that there exists a uniform floating electron gas above the hydrogen atoms in the MXenes such as  $Hf_{n+1}C_n(OH)_2$  ( $n = 1, 2$ , and 3) with partially occupied NFE states. It has been shown that  $Ti_2C(OH)_2$ ,  $Zr_2C(OH)_2$ ,  $Zr_2N(OH)_2$ ,  $Hf_2N(OH)_2$ ,  $Nb_2C(OH)_2$ , and  $Ta_2C(OH)_2$  also possess partially occupied NFE states [42]. The lowest energy NFE states in  $Sc_2C(OH)_2$ ,  $Ti_2N(OH)_2$ , and  $V_2C(OH)_2$  are unoccupied and located above the Fermi energy, but in much lower energy than those of the graphene, graphane, BN, and  $MoS_2$  (see Fig. 6). Therefore, these unoccupied NFE states in OH-terminated MXenes should be accessible more easily than those in other known 2D systems [42].

Similarly to the OH-terminated MXenes, the F- and O-terminated MXenes also exhibit the NFE states. However, the NFE states in the F- and O-terminated MXenes are located at much high energies. For example, as shown in Fig. 6, the lowest energy NFE states of  $Hf_2CF_2$  and  $Hf_2CO_2$  appear around 3 and 5 eV above the Fermi energy, respectively. This already implies that the NFE states of the F- and O-terminated MXenes are not suitable for application purposes. The NFE states in the OH-terminated MXenes are found near the Fermi en-

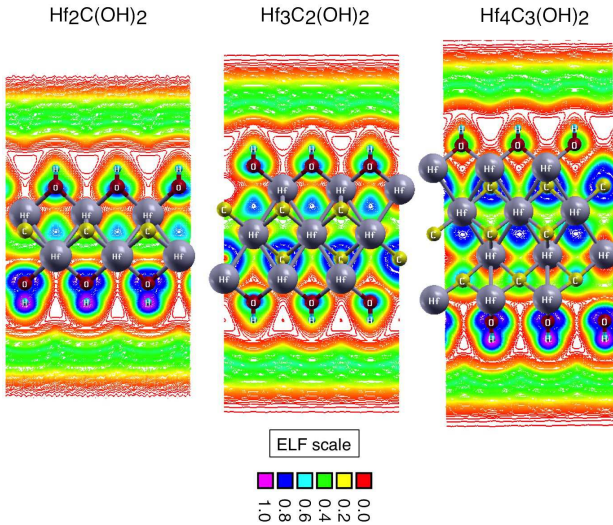


FIG. 7. Electron localization function (ELF) for  $\text{Hf}_{n+1}\text{C}_n(\text{OH})_2$  ( $n=1, 2,$  and  $3$ ) MXenes with different thicknesses [42].

ergy because there exist positively charged hydrogen atoms at the surfaces [42]. As shown in Fig. 7, the presence of the NFE states and the location relative to the Fermi energy do not depend significantly on the thickness of the MXenes. This is simply because the thickness of the MXenes can not essentially change the nature of surface charges, i.e., the surface of the OH-terminated (F and O-terminated) MXenes remains positively (negatively) charged, independently of the thickness.

The partially occupied NFE states near the Fermi energy are sensitive to the circumstances, and indeed they diminish by applying large compressive or tensile strains, adsorbing molecules such as  $\text{O}_2$ ,  $\text{N}_2$ , and  $\text{CO}$ , or heterostructuring the MXenes with graphene, BN, or graphane [42]. It has also been proposed that due to their localized states that appear above the hydrogen atoms, the OH-terminated MXenes may offer potential application toward Pb and heavy metal purification for environmental remediation [30, 31].

#### D. Optical properties

Very few theoretical and experimental studies exist on the optical properties of MXenes. The experimental studies for thin films of  $\text{Ti}_3\text{C}_2\text{T}_x$  (T: mixture of F, OH, or O) are available [18, 19]. It has been observed that  $\text{Ti}_3\text{C}_2\text{T}_x$  obtains 77% transmittance at visible light with wavelength of 550 nm [19]. The intercalated  $\text{Ti}_3\text{C}_2\text{T}_x$  with  $\text{NH}_4\text{HF}_2$  ( $\text{Ti}_3\text{C}_2.3\text{O}_{1.2}\text{F}_{0.7}\text{N}_{0.2}$ ) possesses 90% transmittance, while the transmittance for thin film of the  $\text{Ti}_3\text{AlC}_2$  MAX phase is 30%, which is the least transparent [18]. It has also been observed that the absorbance is linearly dependent on the thickness of the  $\text{Ti}_3\text{C}_2\text{T}_x$  and the intercalated films [18].

Theoretically, optical properties such as transmittance, absorption, and reflection can be evaluated from the imaginary part of the dielectric function tensor calculated as a func-

tion of the photon wavelength [49, 50]. Thus far, the energy loss function, reflectivity, and absorption spectrum of pristine  $\text{Ti}_2\text{C}$ ,  $\text{Ti}_2\text{N}$ ,  $\text{Ti}_3\text{C}_2$ , and  $\text{Ti}_3\text{N}_2$  have been studied. Using the reflectivity and energy loss curves, the plasmon energy is estimated to be 10.00, 11.63, 10.81, and 11.38 eV for these systems listed above, respectively, when the electric field is applied parallel to the surface [49]. It has also been found that, at extremely low energy less than 1 eV, the reflectivity becomes 100% (less than 50%) for these systems when the electric field is applied parallel (perpendicular) to the surface [49]. This indicates the capability of these systems for transmitting electromagnetic waves [49].

In other theoretical studies, the optical properties of pristine and functionalized  $\text{Ti}_2\text{C}$  and  $\text{Ti}_3\text{C}_2$  with F, OH, and O have been examined [50]. It is shown that, in the range of infrared to ultraviolet light including visible light, the in-plane absorption coefficients are lower for the F and OH functionalized MXenes than the bare and O functionalized ones [50]. By analyzing the refractivity, it is concluded that F and OH functionalized  $\text{Ti}_2\text{C}$  and  $\text{Ti}_3\text{C}_2$  should exhibit white color [50].

#### E. Magnetic properties

The spin-polarized density functional calculations indicate that the ground states of the majority of the pristine and functionalized MXenes are nonmagnetic because of the strong covalent bonding between the transition metal and the X element as well as the attached chemical groups. However, the covalency of the bonds can be tuned by applying external strain, which results in the release of  $d$  electrons and consequently the appearance of magnetism even in the otherwise nonmagnetic systems [128].

Many of the pristine MXenes are intrinsically magnetic. For example, pristine  $\text{Ti}_2\text{C}$  and  $\text{Ti}_2\text{N}$  exhibit nearly half-metallic ferromagnetism with the magnetic moments of 1.91 and  $1.00 \mu\text{B}$  per formula unit. The nearly half metallic ferromagnetic monolayer  $\text{Ti}_2\text{C}$  turns into a perfect half-metal, to a spin-gapless semiconductor, and then a metal, under the continuous increase of the biaxial strain, although the monolayer  $\text{Ti}_2\text{N}$  remains nearly half-metallic under the similar biaxial strain [47].

The monolayers of  $\text{V}_2\text{C}$  and  $\text{V}_2\text{N}$  are antiferromagnetic and nonmagnetic metals, respectively. The biaxial tensile and compressive strains induce large magnetic moment in monolayer  $\text{V}_2\text{C}$  and  $\text{V}_2\text{N}$ , respectively [47]. Upon the F or OH functionalization,  $\text{V}_2\text{C}$  becomes a small-gap antiferromagnetic semiconductor [129].

Pristine  $\text{Cr}_2\text{C}$  and  $\text{Cr}_2\text{N}$  are both magnetic. The magnetism results from  $d$  electrons of Cr. The  $\text{Cr}_2\text{C}$  is half-metallic ferromagnetic. However, with the F, Cl, OH, or H functionalization,  $\text{Cr}_2\text{C}$  is transformed to an antiferromagnetic semiconductor [44]. The electronic structure of  $\text{Cr}_2\text{CF}_2$  is shown in Fig. 8.  $\text{Cr}_2\text{N}$  has a larger number of valence electrons than  $\text{Cr}_2\text{C}$ . Hence, in contrast to  $\text{Cr}_2\text{C}$ , the ground state of  $\text{Cr}_2\text{N}$  is antiferromagnetic. However, the half-metallicity appears in  $\text{Cr}_2\text{N}$  upon various surface functionalization with F, O, or OH [130]. This is important because the synthesis of the

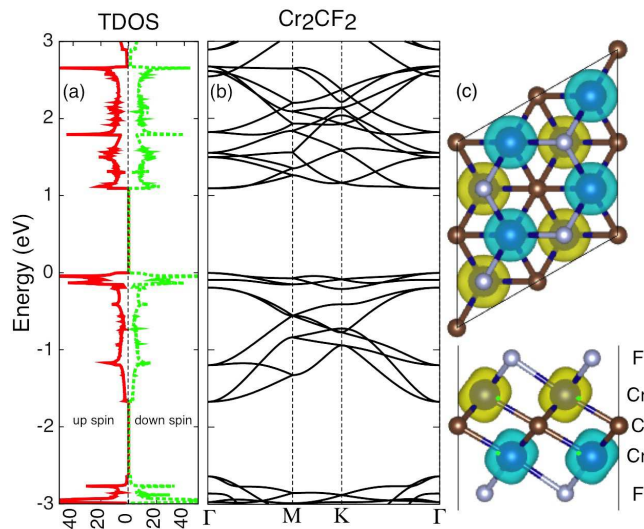


FIG. 8. Electronic structure of antiferromagnetic  $\text{Cr}_2\text{CF}_2$  obtained using the GGA: (a) spin projected density of states [TDOS (states/eV/cell)], (b) band structure, and (c) top and side views of spin density. The Fermi energy is located at zero energy in (a) and (b). Blue and yellow colors indicate spin up and down densities, respectively, in (c).

pristine half-metallic MXenes such as  $\text{Cr}_2\text{C}$  is difficult when the etching technique is employed. It is also found that the energy difference between the magnetic and non-magnetic states of the Cr-based MXenes is so large that these systems might probably keep their magnetism up to near room temperature [39]. Thus, these MXenes are promising materials for spintronic devices.

Recently, non-symmetrically functionalized graphene has been realized and named as Janus graphene [131]. Janus materials possess distinct surfaces because their opposite faces are functionalized with two different chemical groups. Motivated by this, the magnetic properties of MXenes' version of Janus graphene has been studied [45, 46]. It is shown that  $\text{Cr}_2\text{CFCl}$ ,  $\text{Cr}_2\text{CHF}$ ,  $\text{Cr}_2\text{CFOH}$ , and  $\text{V}_2\text{CFOH}$  can be antiferromagnetic semiconductors [45].

There are also attempts to induce magnetism in nonmagnetic MXenes such as  $\text{Sc}_2\text{CT}_2$  ( $T = \text{F}, \text{OH}, \text{and O}$ ) by doping with Ti, V, Cr, or Mn. It is found that Mn and Cr are promising dopants for achieving magnetic  $\text{Sc}_2\text{CT}_2$  [132].

More recently, the magnetic properties of ordered double transition metal carbides MXenes,  $\text{Cr}_2\text{M}''\text{C}_2\text{T}_2$  ( $M'' = \text{Ti and V}, T = \text{F}, \text{OH}, \text{and O}$ ), have been investigated [133]. It is found that  $\text{Cr}_2\text{M}''\text{C}_2\text{T}_2$  can be nonmagnetic, anti-ferromagnetic, or ferromagnetic and either semiconducting or metallic, depending on  $M''$  and  $T$ . It is also shown that  $\text{Cr}_2\text{TiC}_2\text{O}_2$  is nonmagnetic, whereas  $\text{Cr}_2\text{TiC}_2\text{F}_2$  and  $\text{Cr}_2\text{TiC}_2(\text{OH})_2$  are antiferromagnetic, and  $\text{Cr}_2\text{VC}_2(\text{OH})_2$ ,  $\text{Cr}_2\text{VC}_2\text{F}_2$ , and  $\text{Cr}_2\text{VC}_2\text{O}_2$  are ferromagnetic. The Curie temperatures of  $\text{Cr}_2\text{VC}_2(\text{OH})_2$  and  $\text{Cr}_2\text{VC}_2\text{F}_2$  are estimated to be up to 618.36 and 695.65 K, respectively [133]. Another intensive study has found robust ferromagnetism in  $\text{Hf}_2\text{MnC}_2\text{O}_2$  and  $\text{Hf}_2\text{VC}_2\text{O}_2$ , as well as in  $\text{Ti}_2\text{MnC}_2\text{T}_2$  ( $T = \text{F}, \text{OH}, \text{and O}$ ). In these systems, a large mag-

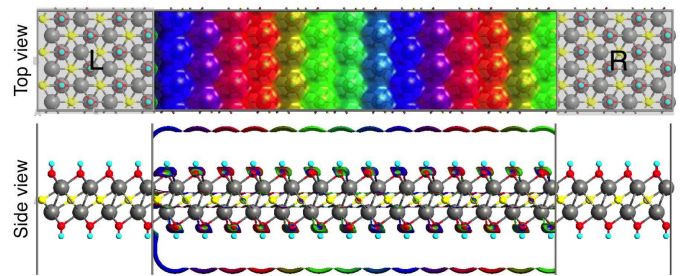


FIG. 9. Top and side views of one of the eigenvectors of transmission matrix with NFE characteristic for  $\text{Hf}_2\text{C}(\text{OH})_2$  [42]. L and R indicate the left and right electrodes, respectively. Since the transmission eigenvector is complex, the absolute value of the eigenvector is shown by the isosurface and the phase is indicated by the color of the isosurface.

netic moment of  $3\text{--}4 \mu\text{B}/\text{cell}$  and a high Curie temperature of  $495\text{--}1133 \text{ K}$  are predicted [134].

## F. Transport properties

There are very few theoretical studies on electron transport properties of the MXenes. The coherent transport calculations using the non-equilibrium Green's function (NEGF) scheme have shown that the metallic MXenes are highly conductive [42, 135]. According to the analyses of pristine and functionalized  $\text{Ti}_3\text{C}_2$ , the type of the surface functionalization has a considerable impact on the electron transport. For example, the current at a given bias voltage in  $\text{Ti}_3\text{C}_2\text{F}_2$  can be up to 4 times larger than that for pristine  $\text{Ti}_3\text{C}_2$  [135]. The current increase is due to the emergence of extended electronic states and also due to the smaller variation of electrostatic profile [135]. Through first-principles calculations, it has been demonstrated that the conduction in stacked of  $\text{Ti}_3\text{C}_2\text{T}_2$  ( $T = \text{F}, \text{OH}, \text{or OH}$ ) is significantly anisotropic due to different effective masses of electrons and holes along different lattice directions [136]. Such anisotropic electronic conduction was evidenced by in situ I-V measurements, in which the in-plane electrical conduction is at least one order of magnitude higher than that vertical to the basal plane [136]. It is also reported that the half metallicity of  $\text{Cr}_2\text{NO}_2$  is robust with 100% polarization for a wide range of applied voltages [130].

Electron transport properties of the MXenes with the partially occupied NFE states have also been studied [42]. The calculations have shown the signature of the NFE states in electron conduction [42]. In general, the better electron transport is expected for the MXenes with the NFE states because these states extend above the MXene surfaces (see Fig. 9) and can conduct electrons through the nearly free channels without being significantly scattered by surface vibrations at finite temperatures. The transmission analysis indeed clearly shows that the NFE states can act as both hole and electron channels at low bias voltages, thus suitable for applications in low-power nanoelectronic devices [42].

The effect of  $\text{NH}_3$ ,  $\text{H}_2$ ,  $\text{CH}_4$ ,  $\text{CO}$ ,  $\text{CO}_2$ ,  $\text{N}_2$ ,  $\text{NO}_2$ , and  $\text{O}_2$  absorption on the electron transport of  $\text{Ti}_2\text{CO}_2$  has also been



investigated theoretically to exploit its potential applications as gas sensor or capturer [57]. Among all these gas molecules, only  $\text{NH}_3$  could be chemisorbed on  $\text{Ti}_2\text{CO}_2$  with apparent charge transfer of 0.174 e. The electron transport exhibits distinct responses with a drastic change of I-V characteristic when  $\text{NH}_3$  is adsorbed on  $\text{Ti}_2\text{CO}_2$ . Thus,  $\text{Ti}_2\text{CO}_2$  could be a promising candidate for  $\text{NH}_3$  sensor with high selectivity and sensitivity [57].

## G. Applications

There have been many proposed applications for the 2D MXenes in literature. Here, we shall focus only on those with electronic and energy harvesting applications.

### 1. Low work function electron emitters

Various metallic substrates of transition metal carbides and nitrides provide the high stability, high melting point, and relatively low work function that have increasingly attracted attentions as suitable field emitters. Considering the properties of the MXenes, members of this family can be good candidates as materials with low work function because of the following two reasons. First, the MXenes offer the tunability of the work function by choosing the proper transition metal as well as the X element, usually carbon or nitrogen. In addition, such compositional tunability provides a possibility to adjust other properties such as thermal, mechanical, and chemical stabilities, and toxicity. Second, during the synthesis of MXenes, their surfaces are functionalized naturally, which changes the electrostatic potential near the surfaces and affects the electronic structures, especially, giving rise to the shift of the Fermi level. These two features have significant effects on the work function [72].

The work function is defined as the energy difference between the Fermi energy and the vacuum level (electrostatic potential away from the surface). From the work function calculations of  $\text{M}_2\text{C}$  and  $\text{M}_{10}\text{C}_9$  ( $\text{M} = \text{Sc}, \text{Ti}, \text{Zr}, \text{Hf}, \text{V}, \text{Nb}, \text{Ta}$ ) as well as  $\text{M}'_2\text{N}$  and  $\text{M}'_{10}\text{N}_9$  ( $\text{M}' = \text{Ti}, \text{Zr}, \text{Hf}$ ) functionalized with F, OH, and O, it is found that the work functions of the bare MXenes and the functionalized ones with F, OH and O are distributed in the range of 3.3–4.8, 3.1–5.8, 1.6–2.8, and 3.3–6.7 eV, respectively [72]. It is also shown that work functions always decrease by the functionalization with OH. This is in remarkable contrast with the systems functionalized with F or O, in which the work functions increase or decrease depending on the type of transition metal. Interestingly,  $\text{M}_2\text{C}(\text{OH})_2$ ,  $\text{M}_{10}\text{C}_9(\text{OH})_2$ ,  $\text{M}'_2\text{N}(\text{OH})_2$  and  $\text{M}'_{10}\text{N}_9(\text{OH})_2$  all exhibit ultralow work functions, as compared with the corresponding bare and the functionalized ones with F and O [72]. The thickness dependences of the work function for  $\text{Ti}_{n+1}\text{C}_n$  ( $n=1-9$ ) functionalized with F, OH and O has been systematically studied, and shown that, regardless of the thickness, a family of  $\text{Ti}_{n+1}\text{C}_n(\text{OH})_2$  exhibits ultralow work function [72].

The work function properties of MXenes can be well understood by the surface dipole moments because the change of

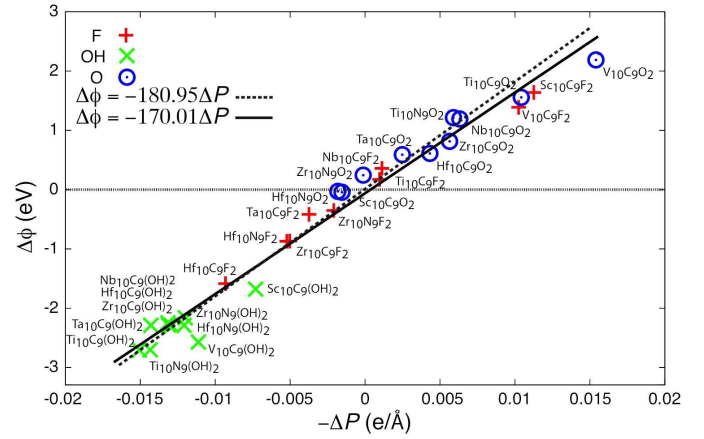


FIG. 10. The change in the work function ( $\Delta\Phi$ ) of  $\text{M}_{10}\text{C}_9$  and  $\text{M}'_{10}\text{N}_9$  ( $\text{M} = \text{Sc}, \text{Ti}, \text{Zr}, \text{Hf}, \text{V}, \text{Nb}, \text{Ta}$ ;  $\text{M}' = \text{Ti}, \text{Zr}, \text{Hf}$ ) functionalized with F, OH, and O as a function of the change in the surface dipole moment ( $\Delta P$ ) [72]. The solid line ( $\Delta\Phi = -170.01\Delta P$ ) indicates the linear fit to the results. The dashed line ( $\Delta\Phi = -180.95\Delta P$ ) is the linear relation reported previously for three-dimensional bulk systems [137].

the work function ( $\Delta\Phi$ ) upon functionalization is linearly correlated with the change of the surface dipole moment ( $\Delta P$ ). It has been shown in Ref. [137] that  $\Delta\Phi = -e/\epsilon_0\Delta P = -180.95\Delta P$  with  $\Delta\Phi = \Phi - \Phi_0$  and  $\Delta P = p - p_0$ . Here,  $e$  (C) is the charge of electron,  $\epsilon_0$  ( $\text{CV}^{-1}\text{\AA}^{-1}$ ) is the vacuum permittivity, and  $\Phi_0$  ( $\Phi$ ) and  $p_0$  ( $p$ ) are the work function and the surface dipole moment without (with) functionalization, respectively. The positive (negative) value of  $\Delta\Phi$  corresponds to the increase (decrease) of the work function when the surface is functionalized. As shown in Fig. 10, MXenes also follow this rule because it is found that  $\Delta\Phi$  correlates with  $\Delta P$  almost linearly with the slope of  $-170.012\text{ V\AA}$  [72].

In general, three main factors control the surface dipole moment upon deposition of any element: i) the redistribution of electron charge between the surface and the adsorbates, ii) the surface relaxation caused by the adsorbates, and iii) the polarity of the adsorbates [72, 137]. Further analysis on the MXenes indicates that the work function of the F and O functionalized MXenes is controlled by two factors, i.e., the dipole moment induced by the charge transfer between F/O and the substrate, and the change of the total surface dipole moment caused by the surface relaxation upon functionalization. Besides these two factors, the intrinsic dipole moment of the OH group plays the most important role in determining the total dipole moment, which consequently justifies the ultralow work function found in the OH terminated MXenes [72].

### 2. Promising catalysts and photocatalysts for hydrogen evolution

Hydrogen is one of the most promising alternative sources of clean energy because the burning of hydrogen produces no pollution [138]. Despite its abundance in water and many hydrocarbons, hydrogen is not found in gas form with high density in nature. A hydrogen evolution reaction (HER)

is the production of hydrogen through the electrocatalysis/photocatalysis process of water or any other inorganic molecules containing hydrogen.

The platinum is one of the most efficient catalysts for hydrogen evolution. However, the usage of platinum is restricted because of its high cost and resource limitation. Recently, MXenes have attracted much attention both experimentally and theoretically because MXenes can be efficient catalysts or photocatalysts for HER. HER activities of  $\text{Ti}_2\text{CT}_x$ ,  $\text{Ti}_3\text{C}_2\text{T}_x$ , and  $\text{Mo}_2\text{CT}_x$  (T: mixture of O and OH) have been measured experimentally [34, 35, 97]. It is found that  $\text{Mo}_2\text{CT}_x$  exhibits a higher HER activity than  $\text{Ti}_2\text{CT}_x$  for hydrogen production from water [35], while  $\text{Ti}_3\text{C}_2\text{T}_x$  can enhance the catalytic activity for hydrogen production from ammonia borane [34]. Theoretically, it is demonstrated that many MXenes are conductive at the standard condition (pH=0). Therefore, this enables MXenes to transfer charge during the HER. Moreover, it is shown theoretically that the Gibbs free energy for the hydrogen absorption on some of the O-terminated MXenes such as  $\text{Ti}_2\text{CO}_2$  and  $\text{W}_2\text{CO}_2$  is close to the ideal value of 0 eV [60, 61]. Considering the Gibbs free energy and the number of electrons captured by oxygen atoms on the O-terminated MXenes, it is predicted that O-terminated MXenes with 0.895–0.977 electron captured per an oxygen atom can be promising 2D catalysts for hydrogen production [60].

More recent theoretical studies have shown that  $\text{M}_2\text{CO}_2$  (M= Ti, Zr, and Hf) exhibits the band gap in the range of 0.92–1.75 eV (calculated using the HSE06 method) [63] with very good light absorbance in the wavelength from 300 to 500 nm [62]. Moreover, it is found that  $\text{Zr}_2\text{CO}_2$  and  $\text{Hf}_2\text{CO}_2$  exhibit high and directionally anisotropic carrier mobility [62]. The large and anisotropic carrier (electron and hole) mobility in these systems facilitate the migration and separation of photogenerated electron-hole pairs [62]. Therefore,  $\text{Zr}_2\text{CO}_2$  and  $\text{Hf}_2\text{CO}_2$  can be used as photocatalyst for hydrogen generation from water [62].

### 3. Energy conversion: thermoelectric devices

Owing to their intrinsic ceramic nature, MXenes may be suitable as thermoelectric materials for energy conversion applications at high temperatures. The performance of thermoelectric material is quantified through the dimensionless figure of merit  $ZT$  given as  $S^2\sigma T/K$ , where  $S$ ,  $\sigma$ ,  $T$ , and  $K$  ( $= k_1 + k_e$ ) are the Seebeck coefficient, electrical conductivity, temperature, and thermal conductivity with both lattice ( $k_1$ ) and electronic ( $k_e$ ) contributions, respectively. Generally,  $ZT$  can be maximized when the power factor ( $S^2\sigma$ ) is maximized and at the same time the thermal conductivity is minimized. The thermal conductivity can be minimized efficiently by enhancing the phonon scattering in the presence of edges, interfaces, grain boundaries, and embedded nanostructures [139]. However, maximizing  $S^2\sigma$  is not straightforward because both  $S$  and  $\sigma$  are strongly coupled to the electronic structure of the system and usually behave inversely: materials that have high Seebeck coefficient have poor electrical conductivity, and vice versa. Therefore, the balance between the Seebeck coefficient

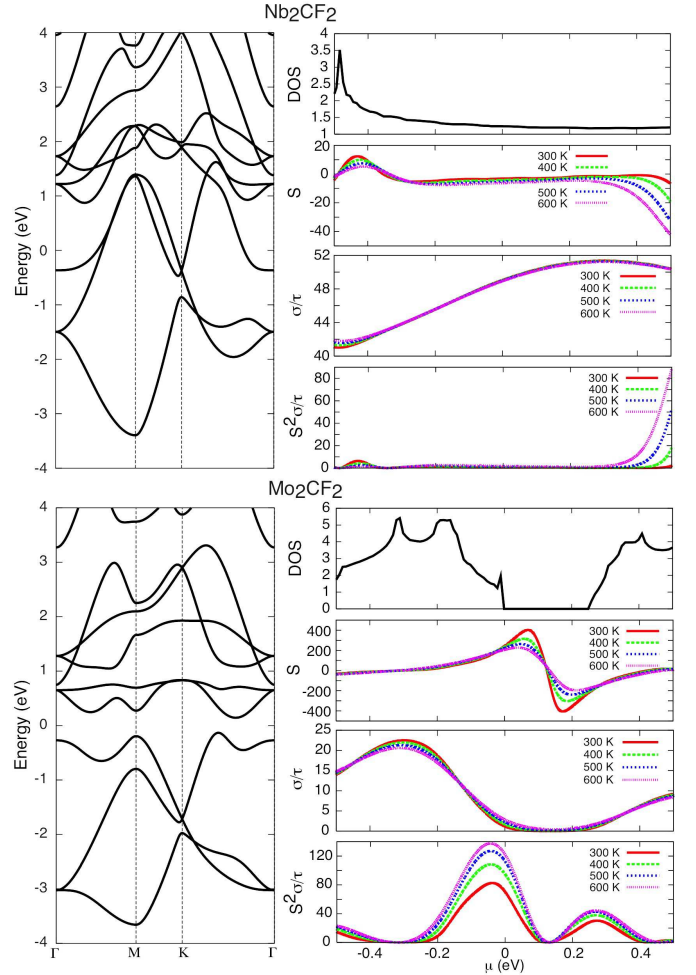


FIG. 11. Band structure, density of states (DOS [states/eV/cell]), Seebeck coefficient ( $S$  [ $\mu\text{VK}^{-1}$ ]), electrical conductivity ( $\sigma/\tau$  [ $10^{17}\Omega^{-1}\text{cm}^{-1}\text{s}^{-1}$ ]), and power factor ( $S^2\sigma/\tau$  [ $10^{14}\mu\text{Wcm}^{-1}\text{K}^{-2}\text{s}^{-1}$ ]) as a function of chemical potential  $\mu$  at various temperatures (indicated in the figures) for  $\text{Nb}_2\text{CF}_2$  (upper panels) and  $\text{Mo}_2\text{CF}_2$  (lower panels) [51]. Here,  $\tau$  is the relaxation time. The band structure and DOS are calculated at zero temperature.  $\mu=0$  corresponds to the Fermi energy at zero temperature in DOS, Seebeck coefficient, electrical conductivity, and power factor.

and the electrical conductivity at a particular p- or n-type carrier concentration is required so as to maximize the power factor.

Based on the Boltzmann theory and first-principles electronic structure calculations, the power factor  $S^2\sigma$  of monolayer and multilayer  $\text{M}_2\text{C}$  (M = Sc, Ti, V, Zr, Nb, Mo, Hf, Ta) and  $\text{M}_2\text{N}$  (M= Ti, Zr, Hf) MXenes functionalized with F, OH, and O groups have already been explored [51]. It has been shown that the metallic (semiconducting) MXenes are poor (good) thermoelectric materials [51]. For example, as shown in Fig. 11 for  $\text{Nb}_2\text{CF}_2$ , the metallic MXenes exhibit excellent electrical conductivity, but very poor Seebeck coefficient, consequently having very poor power factor. On the other hand, the semiconducting MXenes show relatively poor electrical conductivity, but excellent Seebeck coefficient, result-

ing in relatively good power factor. Among the semiconducting MXenes,  $\text{Mo}_2\text{CF}_2$  (see Fig. 11) acquires superior power factor over other MXenes and thus it is potential thermoelectric material in the MXene family [51]. The exceptionally superior thermoelectric property of  $\text{Mo}_2\text{CF}_2$  is attributed to the peculiar band structure near the band edge, where flat and dispersive bands are merged. This type of band shapes allows for a large Seebeck coefficient and simultaneously a good electrical conductivity at low carrier concentrations [140–142].

The thermal conductivity of various MXenes, e.g.,  $\text{M}_2\text{CO}_2$  ( $\text{M} = \text{Ti}, \text{Zr}, \text{Hf}$ ) [52, 55],  $\text{Sc}_2\text{CT}_2$  ( $\text{T} = \text{F}, \text{O}, \text{OH}$ ) [53, 54], and  $\text{Mo}_2\text{C}$  [56], have also been studied by taking into account both phonon and electron contributions. These MXenes are all semiconducting except for pristine  $\text{Mo}_2\text{C}$  that is metallic. The thermal conductivity is in general anisotropic along the armchair and zigzag directions [55]. Among  $\text{M}_2\text{CO}_2$  ( $\text{M} = \text{Ti}, \text{Zr}, \text{Hf}$ ),  $\text{Ti}_2\text{CO}_2$  and  $\text{Hf}_2\text{CO}_2$  exhibit the lowest and highest lattice thermal conductivities, respectively, in the temperature range of 300–700 K. Consequently,  $\text{Ti}_2\text{CO}_2$  achieves a higher figure of merit  $ZT$  for thermoelectric application ( $ZT = 0.45$  for  $14.0 \times 10^{20} \text{ cm}^{-3}$   $n$ -doping and  $ZT = 0.27$  for  $1.7 \times 10^{20} \text{ cm}^{-3}$   $p$ -doping [52]) because of the low thermal conductivity and the high carrier mobility [52, 55]. The room temperature thermal conductivity of  $\text{Hf}_2\text{CO}_2$  is 62.12–131.2 (27.63–53.03)  $\text{Wm}^{-1}\text{K}^{-1}$  along the armchair (zigzag) flake length of 1–100  $\mu\text{m}$  [55]. Among  $\text{Sc}_2\text{CT}_2$  ( $\text{T} = \text{F}, \text{O}, \text{OH}$ ),  $\text{Sc}_2\text{C}(\text{OH})_2$  is predicted to be a candidate for thermoelectric application at elevated temperatures more than 300 K due to a relatively good Seebeck coefficient, high electrical conductivity, and very low lattice thermal conductivity [53]. At room temperature, the thermal conductivity of  $\text{Sc}_2\text{C}(\text{OH})_2$  along the armchair (zigzag) direction can be as large as 123–245 (78.5–148)  $\text{Wm}^{-1}\text{K}^{-1}$  when the flake length increases from 1 to 50  $\mu\text{m}$  [54]. The room temperature thermal conductivity of  $\text{Mo}_2\text{C}$  is also evaluated to be 48.4 (64.7)  $\text{Wm}^{-1}\text{K}^{-1}$  for the armchair (zigzag) flake length of 100  $\mu\text{m}$  [56].

#### 4. Energy storage: hydrogen storage, ion batteries, and supercapacitors

There is a worldwide contest to develop alternative clean energy resources. In this regard, alkali metal batteries, supercapacitors, fuelcells, and hydrogen fuels are among most important candidates, although each of these faces its challenges. For instance, there is a major challenge to find appropriate materials with high storage capacity. 2D materials with large surface areas are most promising for hydrogen storage [143, 144]. The calculations show that pristine  $\text{Sc}_2\text{C}$ ,  $\text{Ti}_2\text{C}$ , and  $\text{V}_2\text{C}$  might be used as hydrogen storage media [64, 65].  $\text{Sc}_2\text{C}$  with the largest surface area among all MXenes possesses the 9.0 wt.%, which is higher than gravimetric storage capacity target, 5.5 wt.% by 2015, set by United States Department of Energy. It has also been shown that the hydrogens are bound to  $\text{Sc}_2\text{C}$  by chemical, physical, and Kubastype interactions with the binding energy of 4.703, 0.087, and 0.164 eV, respectively [65]. Note, however, that when the hydrogens are bound with the surfaces strongly, it is very diffi-

cult to take them out from the storage media. Therefore, these hydrogens cannot be used for the energy production.

Li-ion batteries can produce high gravimetric energy density and high voltage as large as 110–160 Wh/Kg [145] and 3.6 V [146], respectively. Therefore, there are extensive theoretical and experimental studies to design novel alkali-based batteries with high gravimetric energy density and voltage [147–150]. Recently, the intercalation between 2D  $\text{Ti}_3\text{C}_2\text{T}_x$  MXene layers and several ions such as  $\text{Li}^+$ ,  $\text{Na}^+$ ,  $\text{Mg}^{2+}$ ,  $\text{K}^+$ ,  $\text{NH}_4^+$ , and  $\text{Al}^{3+}$  has been reported to induce high capacitance up to 350  $\text{F/cm}^3$  [22]. Moreover, Li ion batteries in  $\text{Ti}_2\text{C}$ ,  $\text{Ti}_3\text{C}_2$ ,  $\text{Ti}_3\text{CN}$ , and  $\text{TiNbC}$  have been experimentally examined [151, 152]. It is found that  $\text{Ti}_3\text{C}_2$  shows excellent Li-ion steady-state capacity of 410  $\text{mAhg}^{-1}$  at a one-cycling rate [152].

These important experimental achievements have triggered many further theoretical studies on supercapacity and alkali-metal ion battery properties of MXenes [26, 129, 153–167]. In these theoretical studies, the effect of functionalization on mobility of various alkali-metals and ions (Li, Na, K, Ca) in pristine MXenes,  $\text{Ti}_2\text{C}$ ,  $\text{Zr}_2\text{C}$ ,  $\text{V}_2\text{C}$ ,  $\text{Nb}_2\text{C}$ ,  $\text{Cr}_2\text{C}$ ,  $\text{Ti}_2\text{N}$ ,  $\text{V}_2\text{N}$ ,  $\text{Ta}_2\text{N}$ ,  $\text{Ti}_3\text{C}_2$ ,  $\text{V}_3\text{C}_2$ , and  $\text{V}_3\text{N}_2$ , as well as functionalized MXenes with F, O, OH, O, S, Se, and Te have been systematically studied. For instance,  $\text{M}_2\text{C}$  ( $\text{M} = \text{Sc}, \text{Ti}, \text{V}, \text{and Cr}$ ) has gravimetric capacity over 400  $\text{mAh/g}$ , which is higher than the gravimetric capacity of graphite [159]. The simulations on Li storage in  $\text{Ti}_3\text{C}_2$  indicate that the pristine MXenes have low diffusion barrier (0.07 eV) and high Li storage capacity [153]. It should be recalled that the Li storage capacity of graphite is 372  $\text{mAh/g}$  in  $\text{LiC}_6$  [153] and the diffusion barrier for Li in graphite is  $\sim 0.3$  eV [168–170]. These facts suggest that the MXenes may be superior to graphite electrodes. However, in functionalized  $\text{Ti}_3\text{C}_2$ , due to steric hindrance induced by F, OH, and O groups, Li ions face higher diffusion barriers as large as 0.36 [153], 1.02 [153], and 0.62 [159] eV, respectively. Consequently, the Li storage in the functionalized MXenes with F, O, and OH decreases as compared with the pristine MXenes. Various theoretical studies have shown that MXenes, particularly pristine ones, are overall promising in increasing the battery performance [26, 153].

## V. NANORIBBON, NANOTUBE, AND HETEROSTRUCTURE MXENES

Although there is no experimental report on the formation of nanotubes, nanoribbons, or hetrostructures of MXenes, there exist many positive signs to expect that they might be realized experimentally. In fact, experiments have observed that MXenes can be formed in the conical scrolls [7], and demonstrated that MXenes can be used as filler in polymer composites [28]. Moreover, the chemical vapor deposition technique can be employed to synthesize MXenes [15]. On the other hand, there have been several theoretical studies on nanoribbon, nanotube, and heterostructure MXenes. For example, the electronic structure and formation energy calculations on pristine and functionalized  $\text{Sc}_2\text{C}$  nanotubes indicate that the stability and the band gap of the MXene nanotubes can be con-

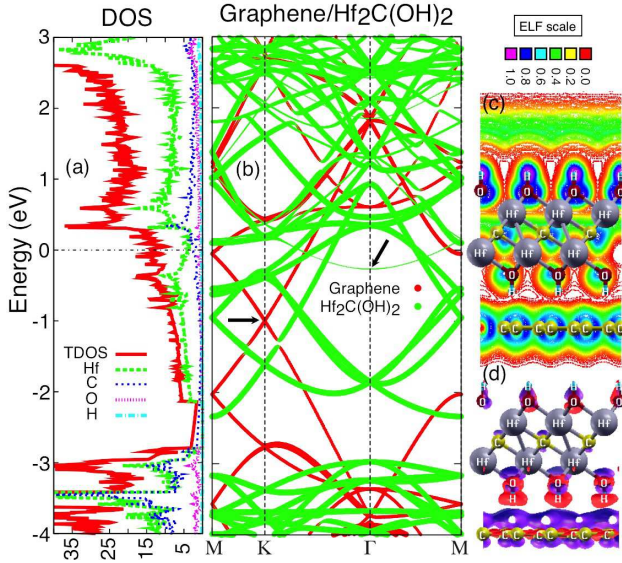


FIG. 12. (a) Density of states (DOS) in states/eV/cell and (b) projected band structure of graphene/Hf<sub>2</sub>C(OH)<sub>2</sub> heterostructure [42]. Arrows in (b) indicate the position of the Dirac cone at the K point and the nearly free electron band band at the  $\Gamma$  point. The Fermi energy is located at zero energy. (c) Electron localization function (ELF) counter plot and (d) charge transfer ( $\Delta\rho$ ) isosurfaces with  $\pm 0.005$  e/Å<sup>3</sup> for graphene/Hf<sub>2</sub>C(OH)<sub>2</sub> [42]. The excess and depleted charges (electrons) are shown in dark orchid and deep pink colors, respectively, in (d).

trolled significantly by their radii [171]. Another study has shown that the strain energies of Ti<sub>2</sub>C nanotubes are always positive, whereas those of Ti<sub>2</sub>CO<sub>2</sub> nanotubes become negative when the diameter is beyond 2.5 nm. This indicates that 2D Ti<sub>2</sub>CO<sub>2</sub> can possibly be folded into a nanotube form [172].

The first-principles calculations for armchair and zigzag nanoribbons of pristine and functionalized Ti<sub>2</sub>C, Ti<sub>3</sub>C<sub>2</sub>, and V<sub>2</sub>C [173] have shown that i) there is a remarkable atomic reconstruction at the edges of nanoribbons, ii) hydrogen functionalization can increase magnetic moment as compared with the pristine nanoribbon, and iii) armchair Ti<sub>2</sub>CO<sub>2</sub> nanoribbon with a width of 7.34 Å exhibits a band gap of  $\sim 1.0$  eV, which is significantly larger than that of 2D Ti<sub>2</sub>CO<sub>2</sub> ( $\sim 0.24$  eV) [39]. It is also shown that the hole and electron carrier mobility of the Ti<sub>2</sub>CO<sub>2</sub> nanoribbon can be tuned by the width as well as the edge engineering [174]. More comprehensive calculations reveal that the band gap of semiconducting MXene nanoribbons is determined by a combination of factors such as the quantum confinement, the energy location of edge states, and the strength of  $d$ - $d$  hybridization [175].

Fabricating van der Waals heterostructures of MXenes, and their stacking with chalcogenides, graphene or other 2D systems can be an innovative route to develop materials with exotic properties. This is promising since similar complex systems have been experimentally realized [176–178]. The basic idea behind the stacking of different 2D layers is the band gap engineering and combining the electronic properties of different 2D layers together into a sin-

gle 3D crystalline composite with substantially tailored electronic properties. For example, the electronic structures of Graphene/Hf<sub>2</sub>C(OH)<sub>2</sub> [42], MoS<sub>2</sub>/Ti<sub>2</sub>C, MoS<sub>2</sub>/Ti<sub>2</sub>CT<sub>2</sub> (T = F and OH) [73], silicene/Sc<sub>2</sub>CF<sub>2</sub> [74], Sc<sub>2</sub>CF<sub>2</sub>/Sc<sub>2</sub>CO<sub>2</sub> [75], and various transition metal dichalcogenides/M<sub>2</sub>CO<sub>2</sub> (M=Sc, Ti, Zr, and Hf) [179, 180] heterostructures have been studied based on first-principles calculations.

Among these studies, it has been found that the transition metal dichalcogenides/Sc<sub>2</sub>CO<sub>2</sub> heterostructures show indirect band gaps in the range of 0.13–1.18 eV, which are suitable for electronic device applications [179]. Figure 12 shows the density of states, projected band structure, excess-depletion charge density ( $\Delta\rho$ ), and electron localization function (ELF) for Graphene/Hf<sub>2</sub>C(OH)<sub>2</sub> heterostructure [42]. These results clearly show that the graphene is  $n$ -doped by Hf<sub>2</sub>C(OH)<sub>2</sub> and this is simply because of the ultra low work function of Hf<sub>2</sub>C(OH)<sub>2</sub> ( $\sim 2.32$  eV) as compared with graphene ( $\sim 4.26$  eV) [42]. However, the Dirac-cone like energy dispersion of the graphene remains intact [see Fig. 12(b)], and is simply shifted to lower energies at  $-1.1$  eV by receiving electrons from Hf<sub>2</sub>C(OH)<sub>2</sub>. Figures 12(c) and 12(d) show that electrons are mainly transferred from OH bonds in Hf<sub>2</sub>C(OH)<sub>2</sub> to  $\pi^*$  states of the graphene. Since the graphene and Hf<sub>2</sub>C(OH)<sub>2</sub> are semi-metallic and metallic, respectively, it is expected that the graphene/Hf<sub>2</sub>C(OH)<sub>2</sub> heterostructure exhibits metallic current-voltage characteristics. Due to the small distance between hydrogen atoms and graphene (2.27 Å), the electrons are localized either on Hf<sub>2</sub>C(OH)<sub>2</sub> or on graphene. However, it is clear that the NFE state remains stable on the other side of Hf<sub>2</sub>C(OH)<sub>2</sub> without graphene. Moreover, the ELF analysis indicates that there is no chemical bond between the graphene and Hf<sub>2</sub>C(OH)<sub>2</sub> [72].

## VI. OUTLOOK

The research on low-dimensional materials is still at a preliminarily stage and will stay as a very exciting field of science and technology for many years. In particular, the MXenes era has just emerged in the cutting-edge materials research arena. It has already been proved that MXenes are suitable materials for interdisciplinary research and collaboration between academia and industry. Synthesizing MXenes with a particular surface functionalization is one of the main experimental challenges in this field. Since some of the MAX phases (Mo<sub>2</sub>GaC) are low temperature superconductors [181], it is timely to examine the superconductivity properties of various MXenes. Our knowledge for photonic properties and solar harvesting applications of MXenes are still limited. It might be possible to grow lateral MXenes using chemical vapor deposition technique. Therefore, it might be interesting to study the lateral MXene heterostructures computationally. It has been demonstrated theoretically that 2D topological insulators might be promising thermoelectric materials [182]. Thus, it is worth examining the thermoelectric properties of the topological MXenes. Catalytic and nanostructure properties of MXenes have not been well studied yet. There are still very few theoretical studies on electron transport, optical, and mag-

netic properties of MXenes. We hope that this review could

provide a broad insight into the current status of research and applications of MXenes, and stimulate further studies.

- 
- [1] Q. H. Wang, K. Kalantar-Zadeh, A. Kis, J. N. Coleman and M. S. Strano, *Nat. Nanotech.*, 2012, **7**, 699.
- [2] S. Z. Butler, S. M. Hollen, L. Cao, Y. Cui, J. A. Gupta, H. R. Gutiérrez, T. F. Heinz, S. S. Hong, J. Huang, A. F. Ismach, E. Johnston-Halperin, M. Kuno, V. V. Plashnitsa, R. D. Robinson, R. S. Ruoff, S. Salahuddin, J. Shan, L. Shi, M. G. Spencer, M. Terrones, W. Windl and J. E. Goldberger, *ACS Nano*, 2013, **7**, 2898.
- [3] G. Fiori, F. Bonaccorso, G. Iannaccone, T. Palacios, D. Neumaier, A. Seabaugh, S. K. Banerjee and L. Colombo, *Nat. Nanotech.*, 2014, **9**, 768.
- [4] G. R. Bhimanapati, Z. Lin, V. Meunier, Y. Jung, J. Cha, S. Das, D. Xiao, Y. Son, M. S. Strano, V. R. Cooper, L. Liang, S. G. Louie, E. Ringe, W. Zhou, S. S. Kim, R. R. Naik, B. G. Sumpter, H. Terrones, F. Xia, Y. Wang, J. Zhu, D. Akinwande, N. Alem, J. A. Schuller, R. E. Schaak, M. Terrones and J. A. Robinson, *ACS Nano*, 2015, **9**, 11509.
- [5] J. N. Coleman, M. Lotya, A. O'Neill, S. D. Bergin, P. J. King, U. Khan, K. Young, A. Gaucher, S. De, R. J. Smith, I. V. Shvets, S. K. Arora, G. Stanton, H. -Y. Kim, K. Lee, G. T. Kim, G. S. Duesberg, T. Hallam, J. J. Boland, J. J. Wang, J. F. Donegan, J. C. Grunlan, G. Moriarty, A. Shmeliov, R. J. Nicholls, J. M. Perkins, E. M. Grieveson, K. Theuvsissen, D. W. McComb, P. D. Nellist and V. Nicolosi, *Science*, 2011, **331**, 568.
- [6] H. Zhang, *ACS Nano*, 2015, **9**, 9451.
- [7] M. Naguib, M. Kurtoglu, V. Presser, J. Lu, J. Niu, M. Heon, L. Hultman, Y. Gogotsi and M. W. Barsoum, *Adv. Mater.*, 2011, **23**, 4248.
- [8] M. Naguib, O. Mashtalir, J. Carle, V. Presser, J. Lu, L. Hultman, Y. Gogotsi and M. W. Barsoum, *ACS Nano*, 2012, **6**, 1322.
- [9] M. F. Cover, O. Warschkow, M. M. M. Bilek and D. R. McKenzie, *J. Phys.: Condens. Matter*, 2009, **21**, 305403.
- [10] Michel W. Barsoum, *Prog. Solid St. Chem.*, 2000, **28**, 201.
- [11] Z. M. Sun, *Int. Mater. Rev.*, 2011, **56**, 143.
- [12] M. Khazaei, M. Arai, T. Sasaki, M. Estili and Y. Sakka, *J. Phys.: Condens. Matter*, 2014, **26**, 505503.
- [13] M. Khazaei, M. Arai, T. Sasaki, M. Estili and Y. Sakka, *Sci. Tech. Adv. Mater.*, 2014, **15**, 014208.
- [14] M. Ashton, R. G. Hennig, S. R. Broderick, K. Rajan and S. B. Sinnott, *Phys. Rev. B*, 2016, **94**, 054116.
- [15] C. Xu, L. Wang, Z. Liu, L. Chen, J. Guo, N. Kang, X. -L. Ma, H. -M. Cheng and W. Ren, *Nat. Mater.*, 2015, **14**, 1135.
- [16] D. Geng, X. Zhao, L. Li, P. Song, B. Tian, W. Liu, J. Chen, D. Shi, M. Lin, W. Zhou and K. P. Loh, *2D Mater.*, 2017, **4**, 011012.
- [17] B. Anasori, Y. Xie, M. Beidaghi, J. Lu, B. C. Hosler, L. Hultman, P. R. C. Kent, Y. Gogotsi and M. W. Barsoum, *ACS Nano*, 2015, **9**, 9507.
- [18] J. Halim, M. Lukatskaya, K. M. Cook, J. Lu, C. R. Smith, L. Å. Näslund, S. J. May, L. Hultman, Y. Gogotsi, P. Eklund and M. W. Barsoum, *Chem. Mater.*, 2014, **26**, 2374.
- [19] M. Mariano, O. Mashtalir, F. Q. Antonio, W. -H. Ryu, B. Deng, F. Xia, Y. Gogotsi and A. D. Taylor, *Nanoscale*, 2016, **8**, 16371.
- [20] Y. Yang, S. Umrao, S. Lai and S. Lee, *J. Phys. Chem. Lett.*, 2017, **8**, 859.
- [21] S. Lai, J. Jeong, S. K. Jang, J. Xu, Y. J. Choi, J. -H. Park, E. Hwang and S. Lee, *Nanoscale*, 2015, **7**, 19390.
- [22] M. R. Lukatskaya, O. Mashtalir, C. E. Ren, Y. Dall'Agnese, P. Rozier, P. L. Taberna, M. Naguib, P. Simon, M. W. Barsoum and Y. Gogotsi, *Science*, 2013, **341**, 1502.
- [23] M. Chidui, M. R. Lukatskaya, M. -Q. Zhao, Y. Gogotsi and M. W. Barsoum, *Nature*, 2014, **516**, 78.
- [24] R. B. Rakhi, B. Ahmed, M. N. Hedhili, D. H. Anjum and H. N. Alshareef, *Chem. Mater.*, 2015, **27**, 5314.
- [25] M. Naguib, J. Halim, J. Lu, K. M. Cook, L. Hultman, Y. Gogotsi and M. W. Barsoum, *J. Am. Chem. Soc.*, 2013, **135**, 15966.
- [26] Y. Xie, Y. Dall'Agnese, M. Naguib, Y. Gogotsi, M. W. Barsoum, H. L. Zhuang and P. R. C. Kent, *ACS Nano*, 2014, **8**, 9606.
- [27] F. Shahzad, M. Alhabeab, C. B. Hatter, B. Anasori, S. M. Hong, C. M. Koo and Y. Gogotsi, *Science*, 2016, **353**, 1137.
- [28] X. Zhang, J. Xu, H. Wang, J. Zhang, H. Yan, B. Pan, J. Zhou and Y. Xie, *Angew. Chem. Int. Ed.* 2013, **52**, 4361.
- [29] M. Xue, Z. Wang, F. Yuan, X. Zhang, W. Wei, H. Tang and C. Li, *RSC Adv.*, 2017, **7**, 4312.
- [30] Q. Peng, J. Guo, Q. Zhang, J. Xiang, B. Liu, A. Zhou, R. Liu and Y. Tian, *J. Am. Chem. Soc.*, 2014, **136**, 4113.
- [31] J. Guo, Q. Peng, H. Fu, G. Zou and Q. Zhang, *J. Phys. Chem. C*, 2015, **119**, 20923.
- [32] J. Chen, K. Chen, D. Tong, Y. Huang, J. Zhang, J. Xue, Q. Huang and T. Chen, *Chem. Commun.*, 2015, **51**, 314.
- [33] O. Mashtalir, K. M. Cook, V. N. Mochalin, M. Crowe, M. W. Barsoum and Y. Gogotsi, *J. Mater. Chem. A*, 2014, **2**, 14334.
- [34] G. Fan, X. Li, Y. Ma, Y. Zhang, J. Wu, B. Xu, T. Sun, D. Gao, and J. Bi, *New J. Chem.*, 2017, DOI: 10.1039/C6NJ02695H.
- [35] Z. W. Seh, K. D. Fredrickson, B. Anasori, J. Kibsgaard, A. L. Strickler, M. R. Lukatskaya, Y. Gogotsi, T. F. Jaramillo, and A. Vojvodic, *ACS Energy Lett.*, 2016, **1**, 589.
- [36] F. Liu, A. Zhou, J. Chen, J. Cao, L. Wang and Q. Hu, *Adsorption*, 2016, **22**, 915.
- [37] J. Ran, G. Gao, F. -T. Li, T. -Y. Ma, A. Du and S. -Z. Qiao, *Nat. Commun.*, 2017, **8**, 13907.
- [38] H. Lin, X. Wang, L. Yu, Y. Chen, and J. Shi, *Nano Lett.*, 2017, **17**, 2017.
- [39] M. Khazaei, M. Arai, T. Sasaki, C. -Y. Chung, N. S. Venkataramanan, M. Estili, Y. Sakka and Y. Kawazoe, *Adv. Funct. Mater.*, 2013, **23**, 2185.
- [40] A. N. Enyashin and A. L. Ivanovskii, *J. Phys. Chem. C*, 2013, **117**, 13637.
- [41] Y. Xie and P. R. C. Kent, *Phys. Rev. B*, 2013, **87**, 235441.
- [42] M. Khazaei, A. Ranjbar, M. Ghorbani-Asl, M. Arai, T. Sasaki, Y. Liang and S. Yunoki, *Phys. Rev. B*, 2016, **93**, 205125.
- [43] L. Feng, X. -H. Zha, K. Luo, Q. Huang, J. He, Y. Liu, W. Deng and S. Du, *J. Electron. Mater.*, 2017, DOI: 10.1007/s11664-017-5311-5.
- [44] C. Si, J. Zhou and Z. Sun, *ACS Appl. Mater. Interfaces*, 2015, **7**, 17510.
- [45] J. He, P. Lyu, L. Z. Sun, Á. M. García and P. Nachtigall, *J. Mater. Chem. C*, 2016, **4**, 6500.

- [46] M. Je, Y. Lee and Y. -C. Chung, *Thin Solid Films*, 2016, **619**, 131.
- [47] G. Gao, G. Ding, J. Li, K. Yao, M. Wu and M. Qian, *Nanoscale*, 2016, **8**, 8986.
- [48] J. Yang, X. Luo, S. Zhang and L. Chen *Phys. Chem. Chem. Phys.*, 2016, **18**, 12914.
- [49] H. Lashgari, M. R. Abolhassani, A. Boochani, S. M. Elahi and J. Khodadadi, *Solid State Commun.*, 2014, **195**, 61.
- [50] Y. Bai, K. Zhou, N. Srikanth, J. H. L. Pang, X. He and R. Wang, *RSC Adv.*, 2016, **6**, 35731.
- [51] M. Khazaei, M. Arai, T. Sasaki, M. Estili and Y. Sakka, *Phys. Chem. Chem. Phys.*, 2014, **16**, 7841.
- [52] A. N. Gandi, H. N. Alshareef and U. Schwingenschlöggl, *Chem. Mater.*, 2016, **28**, 1647.
- [53] S. Kumar and U. Schwingenschlöggl, *Phys. Rev. B*, 2016, **94**, 035405.
- [54] X. -H. Zha, J. Zhou, Y. Zhou, Q. Huang, J. He, J. S. Francisco, K. Luo and S. Du, *Nanoscale*, 2016, **8**, 6110.
- [55] X. -H. Zha, Q. Huang, J. He, H. He, J. Zhai, J. S. Francisco and S. Du, *Sc. Rep.*, 2016, **6**, 27971.
- [56] X. -H. Zha, J. Yin, Y. Zhou, Q. Huang, K. Luo, J. Lang, J. S. Francisco, J. He and S. Du, *J. Phys. Chem. C*, 2016, **120**, 15082.
- [57] X. -F. Yu, Y. Li, J. -B. Cheng, Z. -B. Liu, Q. -Z. Li, W. -Z. Li, X. Yang and B. Xiao, *ACS Appl. Mater. Interfaces*, 2015, **7**, 13707.
- [58] L. -Y. Gan, D. Huang and U. Schwingenschlöggl, *J. Mater. Chem. A*, 2013, **1**, 13672.
- [59] C. Ling, L. Shi, Y. Ouyang, Q. Chen and J. Wang, *Adv. Sci.*, (2016), **3**, 1600180.
- [60] C. Ling, L. Shi, Y. Ouyang and J. Wang, *Chem. Mater.*, 2016, **28**, 9026.
- [61] G. Gao, A. P. O'Mullane and A. Du, *ACS Catal.*, 2017, **7**, 494.
- [62] Z. Guo, J. Zhou, L. Zhua and Z. Sun, *J. Mater. Chem. A*, 2016, **4**, 11446.
- [63] H. Zhang, G. Yang, X. Zuo, H. Tang, Q. Yang, and G. Li, *J. Mater. Chem. A*, 2016, **4**, 12913.
- [64] Q. Hu, H. Wang, Q. Wu, X. Ye, A. Zhou, D. Sun, L. Wang, B. Liu and J. He, *J. Phys. Chem. A*, 2013, **117**, 14253.
- [65] Q. Hu, H. Wang, Q. Wu, X. Ye, A. Zhou, D. Sun, L. Wang, B. Liu and J. He, *Int. J. Hydrogen Energy*, 2014, **39**, 10606.
- [66] J. -J. Zhang and S. Dong, *J. Chem. Phys.*, 2017, **146**, 034705.
- [67] H. Weng, A. Ranjbar, Y. Liang, Z. Song, M. Khazaei, S. Yunoki, M. Arai, Y. Kawazoe, Z. Fang and X. Dai, *Phys. Rev. B*, 2015, **92**, 075436.
- [68] M. Khazaei, A. Ranjbar, M. Arai and S. Yunoki, *Phys. Rev. B*, 2016, **94**, 125152.
- [69] L. Li, *Comput. Mater. Sci.*, 2016, **124**, 8.
- [70] C. Si, K. -H. Jin, J. Zhou, Z. Sun and F. Liu, *Nano Lett.*, 2016, **16**, 6584.
- [71] C. Si, J. You, W. Shi, J. Zhou and Z. Sun, *J. Mater. Chem. C*, 2016, **4**, 11524.
- [72] M. Khazaei, M. Arai, T. Sasaki, A. Ranjbar, Y. Liang and S. Yunoki, *Phys. Rev. B*, 2015, **92**, 075411.
- [73] L. -Y. Gan, Y. -J. Zhao, D. Huang and U. Schwingenschlöggl, *Phys. Rev. B*, 2013, **87**, 245307.
- [74] H. Zhao, C. Zhang, S. Li, W. Ji and P. Wang, *J. Appl. Phys.*, 2015, **117**, 085306.
- [75] Y. Lee, Y. Hwang and Y. C. Chung, *ACS Appl. Mater. Interfaces*, 2015, **7**, 7163.
- [76] Y. Liu, H. Xiao, W. A. Goddard III, *J. Am. Chem. Soc.*, 2016, **138**, 15853.
- [77] H. Fashandi, V. Ivády, P. Eklund, A. L. Spetz, M. I. Katsnelson and I. A. Abrikosov, *Phys. Rev. B*, 2015, **92**, 155142.
- [78] A. L. Ivanovskii and A. N. Enyashin, *Russ. Chem. Rev.*, 2013, **82**, 735.
- [79] Q. Tang, Z. Zhou, and Z. Chen, *WIREs Comput. Mol. Sci.*, 2015, **5**, 360.
- [80] M. Naguib, V. N. Mochalin, M. W. Barsoum, Y. Gogotsi, *Adv. Mater.*, 2014, **26**, 992.
- [81] M. Naguib and Y. Gogotsi, *Acc. Chem. Res.*, 2015, **48**, 128.
- [82] J. -C. Lei, X. Zhang, Z. Zhou, *Front. Phys.*, 2015, **10**, 276.
- [83] V. M. H. Ng, H. Huang, K. Zhou, P. S. Lee, W. Que, Z. J. Xu and L. B. Kong, *J. Mater. Chem. A*, 2016, **5**, 3039.
- [84] B. Anasori, M. R. Lukatskaya, and Y. Gogotsi, *Nat. Rev.*, 2017, **1**, 16098.
- [85] J. P. Perdew, K. Burke, and M. Ernzerhof, *Phys. Rev. Lett.*, 1996, **77**, 3865.
- [86] J. Heyd, G. E. Scuseria, and M. Ernzerhof, *J. Chem. Phys.*, 2006, **124**, 219906.
- [87] S. Baroni, S. de Gironcoli, A. Dal. Corso, and P. Gianozzi, *Rev. Mod. Phys.*, 2001, **73**, 515.
- [88] S. J. Grimme, *Comput. Chem.*, 2006, **27**, 1787.
- [89] A. I. Liechtenstein, V. I. Anisimov and J. Zaane, *Phys. Rev. B*, 1995, **52**, R5467.
- [90] S. L. Dudarev, G. A. Botton, S. Y. Savrasov, C. J. Humphreys and A. P. Sutton, *Phys. Rev. B*, 1998, **57**, 1505.
- [91] A. J. Cohen, P. Mori-Sánchez, and W. Yang, *Science*, 2008, **321**, 729.
- [92] J. F. Nye, 2010, *Physical Properties of Crystals: Their Representation by Tensors and Matrices* (New York: Oxford University Press).
- [93] M. A. Hope, A. C. Forse, K. J. Griffith, M. R. Lukatskaya, M. Ghidui, Y. Gogotsi and C. P. Grey, *Phys. Chem. Chem. Phys.*, 2016, **18**, 5099.
- [94] H. W. Wang, M. Naguib, K. Page, D. J. Wesolowski and Y. Gogotsi, *Chem. Mater.*, 2016, **28**, 349.
- [95] G. Sharma, M. Naguib, D. Feng, Y. Gogotsi and A. Navrotsky, *J. Phys. Chem. C*, 2016, **120**, 28131.
- [96] D. Magne, V. Mauchamp, S. Célérier, P. Chartier and T. Cabioch, *Phys. Chem. Chem. Phys.*, 2016, **18**, 30946.
- [97] K. D. Fredrickson, B. Anasori, Z. W. Seh, Y. Gogotsi and A. Vojvodic, *J. Phys. Chem. C*, 2016, **120**, 28432.
- [98] P. Srivastava, A. Mishra, H. Mizuseki, K. -R. Lee and A. K. Singh, *ACS Appl. Mater. Interfaces*, 2016, **8**, 24256.
- [99] A. Mishra, P. Srivastava, H. Mizuseki, K. -R. Lee and A. K. Singh, *Phys. Chem. Chem. Phys.*, 2016, **18**, 11073.
- [100] R. Meshkini, L. -Å. Näslund and J. Halim, *Scr. Mater.*, 2015, **108**, 147.
- [101] J. Zhou, X. Zha, F. Y. Chen, Q. Ye, P. Eklund, S. Du, and Q. Huang, *Angew. Chem.-Int. Edit.*, 2016, **55**, 5008.
- [102] J. Yang, M. Naguib, M. Ghidui, L. -M. Pan, J. Gu, J. Nanda, J. Halim, Y. Gogotsi and M. W. Barsoum, *J. Am. Ceramic Soc.*, 2016, **99**, 660.
- [103] P. Urbankowski, B. Anasori, T. Makaryan, D. Er, S. Kota, P. L. Walsh, M. Zhao, V. B. Shenoy, M. W. Barsoum and Y. Gogotsi, *Nanoscale*, 2016, **8**, 11385.
- [104] R. Meshkian, Q. Tao, M. Dahlqvist, J. Lu, L. Hultman, J. Rosen, *Acta Mater.*, 2017, **125**, 476.
- [105] M. Ashton, K. Mathew, R. G. Hennig and S. B. Sinnott, *J. Phys. Chem. C*, 2016, **120**, 3550.
- [106] T. Hu, J. Wang, H. Zhang, Z. Li, M. Hu and X. Wang, *Phys. Chem. Chem. Phys.*, 2015, **17**, 9997.
- [107] U. Yorulmaz, A. Özden, N. K. Perkgöz, F. Ay and C. Sevik, *Nanotechnology*, 2016, **27**, 335702.
- [108] M. Kurtoglu, M. Naguib, Y. Gogotsi and M. W. Barsoum, *MRS Commun.*, 2012, **2**, 133.

- [109] X. -H. Zha, K. Luo, Q. Li, Q. Huang, J. He, Xi. Wen and Shiyu Du, *Europhys. Lett.*, 2015, **111**, 26007.
- [110] V. N. Borysiuk, V. N. Mochalin and Y. Gogotsi, *Nanotechnology*, 2015, **26**, 265705.
- [111] Z. Guo, J. Zhou, C. Si and Z. Sun, *Phys. Chem. Chem. Phys.*, 2015, **17**, 15348.
- [112] Z. H. Fu, Q. F. Zhang, D. Legut, C. Si, T. C. Germann, T. Lookman, S. Y. Du, J. S. Francisco and R. F. Zhang, *Phys. Rev. B*, 2016, **94**, 104103.
- [113] T. Hu, M. Hu, Z. Li, H. Zhang, C. Zhang, J. Wang and X. Wang, *Phys. Chem. Chem. Phys.*, 2016, **18**, 20256.
- [114] L. H. Karlsson, J. Birch, J. Halim, M. W. Barsoum and P. O. Å. Persson, *Nano Lett.*, 2015, **15**, 4955.
- [115] X. Sang, Y. Xie, M. -W. Lin, M. Alhabeb, K. L. Van Aken, Y. Gogotsi, P. R. C. Kent, K. Xiao and R. R. Unocic, *ACS Nano.*, 2016, **10**, 9193.
- [116] Z. Guo, L. Zhu, J. Zhou and Z. Sun, *RSC Adv.*, 2015, **5**, 25403.
- [117] Y. Lee, S. B. Cho and Y. -C. Chung, *ACS Appl. Mater. Interfaces*, 2014, **6**, 14724.
- [118] X. -F. Yu, J. -B. Cheng, Z. -B. Liu, Q. -Z. Li, W. -Z. Li, X. Yang and B. Xiao, *RSC Adv.*, 2015, **5**, 30438.
- [119] Y. Lee, Y. Hwang, S. B. Cho and Y. -C. Chung, *Phys. Chem. Chem. Phys.*, 2014, **16**, 26273.
- [120] L. Li, *J. Phys. Chem. C*, 2016, **120**, 24857.
- [121] L. Fu, C. L. Kane and E. J. Mele, Topological insulators in three dimensions, *Phys. Rev. Lett.*, 2007, **98**, 106803.
- [122] L. Fu and C. L. Kane, *Phys. Rev. B*, 2007, **76**, 045302.
- [123] M. Z. Hasan and C. L. Kane, *Rev. Mod. Phys.*, 2010, **82**, 3045.
- [124] X. -L. Qi and S. -C. Zhang, *Rev. Mod. Phys.*, 2011, **83**, 1057.
- [125] B. Yan and S. -C. Zhang, *Rep. Prog. Phys.*, 2012, **75**, 096501.
- [126] H. Weng, R. Yu, X. Hu, X. Dai and Z. Fang, *Adv. Phys.*, 2015, **64**, 227.
- [127] B. Silvi and A. Savin, *Nature*, 1994, **371**, 683.
- [128] S. Zhao, W. Kang and J. Xue, *Appl. Phys. Lett.*, 2014, **104**, 133106.
- [129] J. Hu, B. Xu, C. Ouyang, S. A. Yang and Y. Yao, *J. Phys. Chem. C*, 2014, **118**, 24274.
- [130] G. Wang, *J. Phys. Chem. C*, 2016, **120**, 18850.
- [131] L. Zhang, J. Yu, M. Yang, Q. Xie, H. Peng and Z. Liu, *Nat. Commun.*, 2013, **4**, 1443.
- [132] J. Yang, X. Luo, S. Zhang and L. Chen, *Phys. Chem. Chem. Phys.*, 2016, **18**, 12914.
- [133] J. Yang, X. Zhou, X. Luo, S. Zhang and L. Chen, *Appl. Phys. Lett.*, 2016, **109**, 203109.
- [134] L. Dong, H. Kumar, B. Anasori, Y. Gogotsi and V. B. Shenoy, *J. Phys. Chem. Lett.*, 2017, **8**, 422.
- [135] G. R. Berdiyorov, *Euro. Phys. Lett.*, 2015, **111**, 67002.
- [136] T. Hu, H. Zhang, J. Wang, Z. Li, M. Hu, J. Tan, P. Hou, F. Li and X. Wang, *Sci. Rep.*, 2015, **5**, 16329.
- [137] T. C. Leung, C. L. Kao, W. S. Su, Y. J. Feng and C. T. Chan, *Phys. Rev. B*, 2003, **68**, 195408.
- [138] <http://www.renewableenergyworld.com/hydrogen/tech.html>
- [139] M. Zabarjadi, K. Esfarjani, M. S. Dresselhaus, Z. F. Ren and G. Chen, *Energy Environ. Sci.* 2012, **5**, 5147.
- [140] D. J. Singh and I. I. Mazin, *Phys. Rev. B*, 1997, **56**, 1650.
- [141] A. F. May, D. J. Singh and G. J. Snyder, *Phys. Rev. B*, 2009, **79**, 153101.
- [142] D. J. Singh, *Phys. Rev. B*, 2010, **81**, 195217.
- [143] M. Khazaei, M. S. Bahramy, N. S. Venkataramanan, H. Mizuseki and Y. Kawazoe, *J. Appl. Phys.*, 2009, **106**, 094303.
- [144] NS Venkataramanan, M Khazaei, R Sahara, H Mizuseki and Y Kawazoe, *Chemical Physics*, 2009, **359**, 173.
- [145] D. Linden, T. B. Reddy (eds.), 2001, *Handbook of batteries*. 3rd ed, McGraw-Hill; New York.
- [146] J. -M. Tarascon, *Nat. Chem.*, 2010, **2**, 510.
- [147] K. M. Bui, V. A. Dinh and T. Ohno *Appl. Phys. Exp.*, 2012, **5**, 125802.
- [148] M. S. Islam and C. A. J. Fisher, *Chem. Soc. Rev.*, 2014, **43**, 185.
- [149] K. M. Bui, V. A. Dinh, S. Okadab and Takahisa Ohno, *Phys. Chem. Chem. Phys.*, 2015, **17**, 30433.
- [150] K. M. Bui, V. A. Dinh, S. Okada and T. Ohno, *Phys. Chem. Chem. Phys.*, 2016, **18**, 27226.
- [151] J. Come, M. Naguib, P. Rozier, M. W. Barsoum, Y. Gogotsi, P.-L. Taberna, M. Morcrette and P. Simon, *J. Electrochem. Soc.*, 2012, **159**, A1368.
- [152] O. Mashtalir, M. Naguib, V. N. Mochalin, Y. Dall'Agnesse, M. Heon, M. W. Barsoum and Y. Gogotsi, *Nature Commun.*, 2013, **4**, 1716.
- [153] Q. Tang, Z. Zhou and P. Shen, *J. Am. Chem. Soc.*, 2012, **134**, 16909.
- [154] D. Er, J. Li, M. Naguib, Y. Gogotsi and V. B. Shenoy, *ACS Appl. Mater. Interfaces*, 2014, **6**, 11173.
- [155] Y. Xie, M. Naguib, V. N. Mochalin, M. W. Barsoum, Y. Gogotsi, X. Yu, K. -W. Nam, X. -Q. Yang, A. I. Kolesnikov and P. R. C. Kent, *J. Am. Chem. Soc.*, 2014, **136**, 6385.
- [156] Christopher Eames and M. Saiful Islam, *J. Am. Chem. Soc.*, 2014, **136**, 16270.
- [157] E. Yang, H. Ji, J. Kim, H. Kim and Y. Jung, *Phys. Chem. Chem. Phys.*, 2015, **17**, 5000.
- [158] H. Pan, *J. Mater. Chem. A*, 2015, **3**, 21486.
- [159] M. Ashton, R. G. Hennig and S. B. Sinnott, *Appl. Phys. Lett.*, 2016, 108, 023901.
- [160] X. Ji, K. Xu, C. Chen, B. Zhang, Y. Ruan, J. Liu, L. Miao and J. Jiang, *Phys. Chem. Chem. Phys.*, 2016, **18**, 4460.
- [161] Y. Ando and S. Watanabe, *Appl. Phys. Exp.*, 2016, **9**, 015001.
- [162] Y. -X. Yu, *J. Phys. Chem. C*, 2016, **120**, 5288.
- [163] J. Hu, B. Xu, C. Ouyang, Y. Zhang and S. A. Yang, *RSC Adv.*, 2016, **6**, 27467.
- [164] L. Bai, H. Yin and X. Zhang, *RSC Adv.*, 2016, **6**, 54999.
- [165] F. Li, C. R. Cabrera, J. Wang and Z. Chen, *RSC Adv.*, 2016, **6**, 81591.
- [166] J. Zhu, A. Chroneos, J. Eppinger and U. Schwingenschlögl, *App. Mater. Today*, 2016, **5**, 19.
- [167] X. Chen, Z. Kong, N. Li, X. Zhao and C. Sun, *Phys. Chem. Chem. Phys.*, 2016, **18**, 32937.
- [168] K. Persson, Y. Hinuma, Y. S. Meng, A. Van der Ven and G. Ceder, *Phys. Rev. B*, 2010, **82**, 125416.
- [169] K. Toyoura, Y. Koyama, A. Kuwabara and I. Tanaka, *J. Phys. Chem. C*, 2010, 114, 2375.
- [170] K. Persson, V. A. Sethuraman, L. J. Hardwick, Y. Hinuma, Y. S. Meng, A. van der Ven, V. Srinivasan, R. Kostecki and G. Ceder, *J. Phys. Chem. Lett.*, 2010, **1**, 1176.
- [171] X. Zhang, Z. Ma, X. Zhao, Q. Tang and Z. Zhou, *J. Mater. Chem. A*, 2015, **3**, 4960.
- [172] X. Guo, P. Zhang and J. Xue, *J. Phys. Chem. Lett.*, 2016, **7**, 5280.
- [173] S. Zhao, W. Kang and J. Xue, *J. Mater. Chem. C*, 2015, **3**, 879.
- [174] X. Zhang, X. Zhao, D. Wu, Y. Jing and Z. Zhou, *Nanoscale*, 2015, **7**, 16020.
- [175] H. Hong, R. F. Klie and S. Ogut, *Phys. Rev. B*, 2016, **93**, 115412.
- [176] L. A. Ponomarenko, A. K. Geim, A. A. Zhukov, R. Jalil, S. V. Morozov, K. S. Novoselov, I. V. Grigorieva, E. H. Hill, V. V. Cheianov, V. I. Fal'ko, K. Watanabe, T. Taniguchi and R. V. Gorbachev, *Nature Phys.*, 2011, **7**, 958.
- [177] L. Britnell, R. V. Gorbachev, R. Jalil, B. D. Belle, F. Schedin, M. I. Katsnelson, L. Eaves, S. V. Morozov, N. M. R. Peres, J.

- Leist, A. K. Geim, K. S. Novoselov and L. A. Ponomarenko, *Science*, 2012, **335**, 947.
- [178] A. K. Geim and I. V. Grigorieva *Nature*, 2013, **499**, 419.
- [179] Z. Ma, Z. Hu, X. Zhao, Q. Tang, D. Wu, Z. Zhou and L. Zhang, *J. Phys. Chem. C*, 2014, **118**, 5593.
- [180] A. N. Gandi, H. N. Alshareef and U. Schwingenschlögl, *J. Phys.: Condens. Mater.*, 2017, **29**, 035504.
- [181] W. Jeitschko, H. Nowotny and F. Benesovsky, *Monatsh. Chem.*, 1963, **94**, 672.
- [182] Y. Xu, Z. Gan and S. -C. Zhang, *Phys. Rev. Lett.*, 2014, **112**, 226801.